J. Fluid Mech. (2024), *vol*. 979, A20, doi:10.1017/jfm.2023.1061

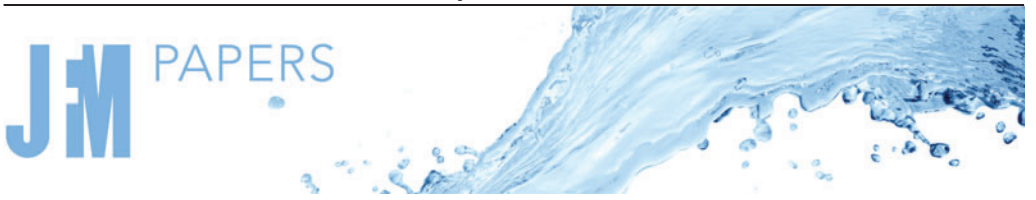

Reynolds number effects on a velocity–vorticity correlation-based skin-friction drag decomposition in incompressible turbulent channel flows

Yunchao Zhao[1], **Yitong Fan**[1,2] **and Weipeng Li**[1,†]

[1]School of Aeronautics and Astronautics, Shanghai Jiao Tong University, Shanghai 200240, PR China

[2]Department of Mechanical Engineering, University of Melbourne, Parkville, VIC 3010, Australia

(Received 3 May 2023; revised 19 November 2023; accepted 6 December 2023)

A form of skin-friction drag decomposition is given based on the velocity–vorticity correlations, $\langle v\omega_z\rangle$ and $\langle -w\omega_y\rangle$, which represent the advective vorticity transport and vortex stretching, respectively. This identity provides a perspective to understand the mechanism of skin-friction drag generation from vortical motions and it has better physical interpretability compared with some previous studies. The skin-friction coefficients in incompressible turbulent channel flows at friction Reynolds numbers from 186 to 2003 are divided with this velocity–vorticity correlation-based identity. We mainly focus on the Reynolds number effects on the contributing terms, their scale-dependence and quadrant characteristics. Results show that the contributing terms and their proportions exhibit similarities and the same peak locations across the wall layer. For the first time, we find that the positive and negative regions in the spanwise pre-multiplied spectra of the turbulent inertia ($\langle v'\omega_z'\rangle + \langle -w'\omega_y'\rangle$) can be separated with a universal linear relationship of $\lambda_z^+ = 3.75y^+$. The linear relationship is adopted as the criterion to investigate the scale dependence of the velocity–vorticity coupling structures. It reveals that the negative and positive structures dominate the generation of friction drag associated with the advective vorticity transport and vortex stretching, respectively. Moreover, quadrant analyses of the velocity–vorticity correlations are performed to further examine the friction drag generation related to different quadrant motions.

Key words: channel flow, turbulence theory

† Email address for correspondence: liweipeng@sjtu.edu.cn

1. Introduction

The friction drag generated by intense turbulent wall-shear stresses exists in numerous engineering and environmental wall-bounded flows, leading to immense economic costs. For instance, a 1 % drag reduction for a long-range transport aircraft could increase the payload by 91 kg at the cruise condition (Meredith 1993; Fan & Li 2019). Therefore, the reduction of turbulent friction drag is of great importance for energy saving and commercial value. Strategies to reduce the turbulent friction drag have long been pursued in industrial designs, which require profound understanding on the generation mechanisms and contributing factors of the friction drag in wall-bounded turbulence.

By definition, the mean skin-friction drag is the mean shear stress on the wall surface. In wall-bounded turbulent flows, the near-wall turbulent events are pronouncedly impacted by the motions in the logarithmic and outer region, especially the large-scale motions (LSMs) and very-large-scale motions (VLSMs) by means of superposition and modulation (Hoyas & Jiménez 2006; Mathis *et al.* 2009). For this reason, it is reasonable that the generation of mean skin-friction drag is related to the flow motions and quantities across the whole layer. The first breakthrough towards this theme was made by Fukagata, Iwamoto & Kasagi (2002), who derived a concise identity (referred to as FIK identity) of skin-friction coefficient C_f by performing triple integration on the streamwise Reynolds-averaged Navier–Stokes (RANS) equation. For fully developed turbulent channel flows, on the premise of homogeneity in streamwise and spanwise directions, the identity is simplified as

$$C_f = \underbrace{6\int_0^1 (1-y)\langle -u'v'\rangle \,\mathrm{d}y}_{C_{f1,FIK}} + \underbrace{\frac{6}{Re_b}}_{C_{f2,FIK}}. \tag{1.1}$$

Herein, the streamwise, wall-normal and spanwise directions are denoted by x, y and z, respectively, and the corresponding velocity components are u, v and w. All quantities in (1.1) are normalized with u_b^* and h^*, where u_b^* is bulk velocity and h^* is the half-channel height. Additionally, $Re_b = u_b^* h^*/\nu^*$ is the bulk Reynolds number and ν^* is kinematic viscosity. The superscript * denotes a dimensional variable. The angle bracket $\langle\rangle$ represents averaging over homogeneous directions (streamwise and spanwise directions) and time, and primed quantities refer to the fluctuations. In the FIK identity, $C_{f1,FIK}$ is the integral of the Reynolds stress weighted by $(1-y)$, which measures contribution from turbulent motions, and $C_{f2,FIK}$ is identical to the well-known laminar solution. Renard & Deck (2016) provided another identity to decompose the skin friction based on the mean streamwise kinetic-energy budget in an absolute reference frame (named as RD identity). In their framework, C_f in turbulent channel flows is attributed to the molecular-viscous-dissipation contribution and the production of the turbulent kinetic energy.

The FIK and RD identity have been popularly utilized, and alternative forms and modifications have emerged gradually in the literature. Gomez, Flutet & Sagaut (2009) derived a compressible form of the FIK identity to investigate the compressibility effects on skin-friction drag generation. Bannier, Garnier & Sagaut (2015) extended the FIK identity to complex wall surfaces and investigated the drag-reduction mechanism of riblet-mounted surfaces. Kametani & Fukagata (2011) and Kametani *et al.* (2015) investigated the turbulent boundary layer with wall blowing/suction and evaluated contributions of each term in the FIK identity. Ricco & Skote (2022) proposed several alternative integral relations and discussed the feasibility of an arbitrary-fold multiple integral. Wenzel, Gibis & Kloker (2022) employed a twofold integral to obtain

improved FIK-like decomposition identities of C_f and C_h (the heat-transfer coefficient). Analogously, Xu, Wang & Chen (2022) applied an FIK-like decomposition to investigate the streamwise evolutions of C_f and C_h in hypersonic transitional and turbulent boundary layers. Other applications and modifications of the FIK identity can be found from Mehdi & White (2011), Mehdi *et al.* (2013), Peet & Sagaut (2009) and Modesti *et al.* (2018), to name a few. When it comes to the RD identity, it gives an edge in interpreting skin-friction generation from the view of energy balance and has also been further developed in recent years. Wei (2018) verified it in three canonical turbulent wall-bounded flows using direct numerical simulation (DNS) and experimental data. Li *et al.* (2019) and Fan, Li & Pirozzoli (2019*b*), Fan *et al.* (2020) extended it to compressible turbulent channel flows, zero- and adverse-pressure-gradient boundary layers. Additionally, Fan *et al.* (2022) employed it to investigate the effects of uniform blowing and suction on the generation of skin friction over an airfoil.

It is noteworthy that Yoon *et al.* (2016) proposed a velocity–vorticity-based method of skin-friction decomposition by performing triple integration on the mean spanwise vorticity transport equation. For turbulent channel flows, it is expressed as

$$C_f = \underbrace{\int_0^1 2(1-y)\langle v'\omega_z'\rangle \,\mathrm{d}y}_{C_{f1,Yoon}} + \underbrace{\int_0^1 2(1-y)\langle -w'\omega_y'\rangle \,\mathrm{d}y}_{C_{f2,Yoon}} + \underbrace{\frac{1}{Re_b}\frac{\mathrm{d}\langle\omega_z\rangle}{\mathrm{d}y}\bigg|_{y=0}}_{C_{f3,Yoon}} \underbrace{-\frac{1}{Re_b}\int_0^1 2\langle\omega_z\rangle \,\mathrm{d}y}_{C_{f4,Yoon}}, \quad (1.2)$$

where vorticities in streamwise, wall-normal and spanwise directions are denoted by ω_x, ω_y and ω_z. This identity provides a tool to understand the mechanism of skin-friction generation from the perspective of vortical motions, yielding contributions of advective vorticity transport ($C_{f1,Yoon}$), vortex stretching ($C_{f2,Yoon}$) by integrals of velocity-vorticity correlation, and the viscous effects of the mean vorticity ($C_{f3,Yoon}$ and $C_{f4,Yoon}$). A relevant further application of this identity was carried out in adverse-pressure-gradient turbulent boundary layers to identify contributions from the large-scale velocity–vorticity correlated motions to the skin-friction drag (Yoon, Hwang & Sung 2018).

Actually, one can perform a fourfold integration $\int_0^1\int_0^y\int_0^{y_3}\int_0^{y_2}\mathrm{d}y_1\,\mathrm{d}y_2\,\mathrm{d}y_3\,\mathrm{d}y$ (where y, y_1, y_2 and y_3 are all wall-normal distances) on the mean spanwise vorticity equation, to reduce Yoon's identity to the FIK identity (see Appendix A). However, it is argued that the triple integral applied in the derivation of the FIK identity has no clear physical interpretations, including a dimensional problem and a weight factor $(1-y)$ of Reynolds stress (Renard & Deck 2016; Wenzel *et al.* 2022). On one hand, the second integral multiplies a force (from the first integral) by length and this should have the dimension of an energy, rather than a velocity as stated by Fukagata *et al.* (2002). On the other hand, the weight factor $(1-y)$ in $C_{f1,FIK}$ results from the mathematical derivation (the third integral) and has no clear explanation in terms of physical processes (Deck *et al.* 2014; Renard & Deck 2016; Fan, Cheng & Li 2019*a*; Li *et al.* 2019; Fan *et al.* 2020). It magnifies the weight of flow information in the near-wall region and attenuates that in the outer layer, which may require high spatial resolution and accuracy in the vicinity of wall-surface for both experimental measurements and numerical simulations (Xia, Zhang & Yang 2021). Moreover, Wenzel *et al.* (2022) declared that an arbitrary-fold integral would result in an FIK-like identity according to Cauchy's formula for repeated integration. Zhang & Xia (2020) and Wenzel *et al.* (2022) pointed out that the twofold integral has a more intuitive physical interpretability than the threefold one on account of the absence of the weight factor $(1-y)$ in channel flows. In (1.2), the ill-defined weight factor $(1-y)$ also appears in the first two terms, which is consistent with the FIK identity due to the analogous integration performed. Therefore, in this study, we give an alternative form of skin-friction

drag decomposition based on the velocity–vorticity correlation. Although it resembles the identity proposed by Yoon *et al.* (2016), to some extent, better physics-informed interpretation could be inferred in this form since it does not suffer from the weight factor $(1 - y)$ in the integrand.

Additionally, the velocity–vorticity correlations appearing in (1.2), $\langle v'\omega_z'\rangle$ and $\langle -w'\omega_y'\rangle$, play important roles in the dynamics of vortical motions. Tennekes & Lumley (1972) first uncovered that $\langle v'\omega_z'\rangle$ is associated with the vortex transport and $\langle -w'\omega_y'\rangle$ with the vortex stretching. Simultaneously, $\langle -w'\omega_y'\rangle$ is hypothesized to be the key factor driving the energy cascade and angular momentum transferring from large eddies to small ones (Tennekes & Lumley 1972; Priyadarshana *et al.* 2007). In incompressible turbulent flows, there exists a relationship to combine $\langle v'\omega_z'\rangle$ and $\langle -w'\omega_y'\rangle$ into the turbulent inertia (TI), i.e.

$$\frac{\mathrm{d}\langle -u'v'\rangle}{\mathrm{d}y} = \langle v'\omega_z'\rangle + \langle -w'\omega_y'\rangle. \tag{1.3}$$

TI is the gradient of the Reynolds shear stress in the wall-normal direction. It derives from the time rate of change of momentum (i.e. inertial) part of the RANS equation (Chin *et al.* 2014). In the mean momentum equation, TI acts as the momentum source in the near-wall region and the momentum sink in the outer layer. Equation (1.3) connects the mean wall-normal transport of Reynolds shear stress with the vorticity field (Klewicki 1989) and provides a way to understand the generation of TI (Guerrero, Lambert & Chin 2022). Klewicki (2013) evidenced the coexistence of dynamical and vortical processes, in which the wall-ward momentum transport occur simultaneously with the outward vorticity transport (dominated by mean spanwise vorticity $\langle\omega_z\rangle$) under the same physical mechanisms. Three-dimensional vortical structures populate through the whole flow field especially in the near-wall region, which indicates that the generation of skin-friction drag is closely related to the vortical motions. In this sense, Yoon's identity in (1.2) indeed provides an effective idea to investigate their relationship.

Another objective in this study is to investigate the Reynolds number effects on the skin-friction-drag generation from the perspective of vortex dynamics. As the Reynolds number increases, the outer scales (characterized by h^* and u_b^*) are increasingly larger than the inner scales (characterized by viscous length scale δ_ν^* and friction velocity u_τ^*) (Priyadarshana *et al.* 2007). The contribution of the near-wall small-scale structures to the skin-friction generation is attenuated, while that of the large-scale motions is enhanced due to the more intense amplitude modulation and energy superposition effects (Hwang 2013). Fan *et al.* (2019*a*) studied the Reynolds number effects on the terms in the FIK and RD identity in turbulent channel flows up to $Re_\tau = 5200$ (where $Re_\tau = u_\tau^* h^*/\nu^*$ is the friction Reynolds number). Chin *et al.* (2014) demonstrated that the streamwise pre-multiplied co-spectra $\phi_{v'\omega_z'}$ scaled in inner units exhibits invariance with Re_τ, whereas $\phi_{-w'\omega_y'}$ shows non-negligible variations with Re_τ.

Based on the aforementioned issues, we are motivated to give a skin-friction drag decomposition method with more intuitive physical interpretability using velocity–vorticity correlations, and quantify the contribution as well as investigate the Reynolds number effects of each individual term. The rest of this paper is organized as follows. Mathematical derivation and physical explanations are introduced in § 2. Details of direct numerical simulations of five turbulent channel cases are described in § 3. In § 4, statistical properties of the decomposed components, including absolute contribution values and proportions, local large- and small-scale motions contributions, and quadrant characteristics, are investigated. Particular attention is paid to the effects of

Reynolds number on the velocity–vorticity integral terms. Finally, concluding remarks are summarized in § 5.

2. Mathematical approach

The equation of the streamwise mean momentum balance for fully developed incompressible turbulent channel flows is expressed as

$$\frac{\mathrm{d}\langle -u'v'\rangle}{\mathrm{d}y}+\frac{1}{Re_b}\frac{\mathrm{d}^2\langle u\rangle}{\mathrm{d}y^2}+\frac{1}{Re_b}\frac{\mathrm{d}\langle u\rangle}{\mathrm{d}y}\bigg|_{y=0}=0. \tag{2.1}$$

Hereafter, variables without the superscript * represent non-dimensional quantities normalized by bulk mean velocity u_b^* and half-channel height h^*, and variables with the superscript '+' represent non-dimensional quantities normalized by friction velocity u_τ^* and viscous length scale δ_v^*, unless otherwise mentioned. With $\langle v\omega_z\rangle=\langle v'\omega_z'\rangle$ and $\langle -w\omega_y\rangle=\langle -w'\omega_y'\rangle$, (1.3) can be re-expressed as

$$\frac{\mathrm{d}\langle -u'v'\rangle}{\mathrm{d}y}=\langle v\omega_z\rangle+\langle -w\omega_y\rangle. \tag{2.2}$$

Substituting (2.2) into (2.1) and integrating in the wall-normal direction from 0 (wall surface) to an arbitrary height $y\in(0,1]$, we get

$$\int_0^y\langle v\omega_z\rangle\,\mathrm{d}y+\int_0^y\langle -w\omega_y\rangle\,\mathrm{d}y=-\frac{1}{Re_b}\frac{\mathrm{d}\langle u\rangle}{\mathrm{d}y}+\frac{1}{Re_b}\frac{\mathrm{d}\langle u\rangle}{\mathrm{d}y}\bigg|_{y=0}-\frac{1}{Re_b}y\frac{\mathrm{d}\langle u\rangle}{\mathrm{d}y}\bigg|_{y=0}. \tag{2.3}$$

The skin-friction coefficient is defined as $C_f=\langle\tau_w^*\rangle/(\frac{1}{2}\rho^*u_b^{*2})$, where $\tau_w^*=\mu^*(\partial u^*/\partial y^*)|_{y=0}$ is the wall-shear stress, μ^* is the dynamic viscosity and ρ^* is the density. It has an alternative form $C_f=2(\mathrm{d}\langle u\rangle/\mathrm{d}y)|_{y=0}/Re_b$. Substituting it into (2.3), we have

$$C_f=\underbrace{2\int_0^y\langle v\omega_z\rangle\,\mathrm{d}y}_{C_{f1}}+\underbrace{2\int_0^y\langle -w\omega_y\rangle\,\mathrm{d}y}_{C_{f2}}+\underbrace{\frac{2}{Re_b}\frac{\mathrm{d}\langle u\rangle}{\mathrm{d}y}}_{C_{f3}}+\underbrace{\frac{2}{Re_b}y\frac{\mathrm{d}\langle u\rangle}{\mathrm{d}y}\bigg|_{y=0}}_{C_{f4}}. \tag{2.4}$$

The first two terms C_{f1} and C_{f2} measure the contribution from advective vorticity transport and vortex stretching throughout the height interval $[0,y]$ uniformly. Additionally, C_{f3} represents the non-dimensional mean streamwise shear stress at height y, i.e. $\langle\tau^*\rangle(y)/(\frac{1}{2}\rho^*u_b^{*2})$, and C_{f4} is simply yC_f that will be discussed later. Equation (2.4) can be generalized to the cases of turbulent pipe and boundary layer flows, which are introduced in Appendices C and D, respectively.

Several remarks about (2.4) need to be elucidated. Initially, the first two terms on the right-hand side, C_{f1} and C_{f2}, are exactly equivalent to the Reynolds shear stress (two times) at height y. Decomposing the Reynolds stress into C_{f1} and C_{f2} provides a way to understand how the vortical motions fundamentally contribute to the skin friction. For the integral in C_{f1} and C_{f2}, the upper bound is not necessarily 1 (Mehdi *et al.* 2013) and even the lower bound is not necessarily 0 (Xia *et al.* 2021). In this study, integration from the wall surface to an arbitrary height is applied to weight all contributions in this interval.

Additionally, by multiplying $(1-y)$ and integrating in y over $[0,1]$, (2.4) is transformed to the standard FIK identity (1.1) (see Appendix B), indicating that they are intrinsically consistent. The typical difference between (2.4) and other classic skin-friction coefficient

Case	Re_τ	Re_b	N_x	N_z	N_y	L_x^*/h^*	L_z^*/h^*	L_y^*/h^*	Δy^+_{min}	Δy^+_{max}
*Re*180	186	2928	768	512	97	12π	4π	2	0.0964	5.89
*Re*350	359	6219	1024	768	193	8π	3π	2	0.0469	5.73
*Re*550	547	10 060	1536	1536	257	8π	4π	2	0.0412	6.71
*Re*950	934	18 535	3072	2304	385	8π	3π	2	0.0313	7.64
*Re*2000	2003	43 635	6144	4608	633	8π	3π	2	0.323	8.89

Table 1. Simulation parameters of the DNS database. Here, N_x, N_z and N_y are grid numbers in the streamwise, spanwise and wall-normal direction, respectively; L_x^*, L_z^* and L_y^* are sizes of the computation domain in three directions. The Δy^+_{min} and Δy^+_{max} are the finest and coarsest grid spacings in the wall-normal direction.

identifiers, such as proposed by Mehdi *et al.* (2013), Yoon *et al.* (2016) and Ricco & Skote (2022), is the absence of integrand factor $(1-y)$, or equivalently, one less performance of integration over [0, 1] (Ricco & Skote 2022; Wenzel *et al.* 2022). As mentioned in the introduction, these FIK-like identities suffer from the ill-defined physical interpretation caused by the factor $(1-y)$ in the integrand. Here, (2.4) without $(1-y)$ evaluates contributions at each height uniformly.

One may be confused by C_{f4} in (2.4), as it is simply yC_f. An explicit expression could be obtained if we move C_{f4} to the left-hand side of (2.4). However, this will cause singularity at $y=1$. According to the derivation in Appendix A, we find an equality relation: $(\mathrm{d}\langle u\rangle/\mathrm{d}y)|_{y=0} = (\mathrm{d}\langle\omega_z\rangle/\mathrm{d}y)|_{y=0}$. The last term in (2.4) can be rewritten as $C_{f4} = (2/Re_b)y(\mathrm{d}\langle\omega_z\rangle/\mathrm{d}y)|_{y=0}$. In this sense, C_{f4} can be explained as the weighted mean vorticity gradient at the wall. The weight factor y is the consequence of wall-normal integration to an arbitrary height. Therefore, C_{f4} could also be interpreted as the accumulative effect of the wall-surface mean vorticity gradient below y. The expression $C_{f4} = (2/Re_b)y(\mathrm{d}\langle\omega_z\rangle/\mathrm{d}y)|_{y=0}$ is akin to $C_{f3,Yoon} = (1/Re_b)(\mathrm{d}\langle\omega_z\rangle/\mathrm{d}y)|_{y=0}$ in the study by Yoon *et al.* (2016). They interpreted $C_{f3,Yoon}$ as 'the viscous effects of the mean vorticity, i.e. the molecular diffusion at the wall'. Term $C_{f3,Yoon}$ is not weighted by y, as the outermost integral of the triple integration was performed from the wall to the central plane.

As a final note about (2.4), the derivation of (2.4) requires: (i) the homogeneity in the streamwise and spanwise directions; and (ii) the zero mean of v and w at each height. Therefore, (2.4) is unable to handle cases that do not meet these two requirements, for instance, turbulent flows with wall blowing/suction or riblet-mounted surfaces.

3. DNS database

We use the DNS database of turbulent channel flows built by Jiménez (Del Álamo & Jiménez 2003; Del Álamo *et al.* 2004; Hoyas & Jiménez 2006). Five cases covering a relatively wide Reynolds number range ($Re_\tau = 186-2003$) are taken into account. Simulation parameters are summarized in table 1. It has been demonstrated that the scale of VLSMs is no larger than around $2h^*$ in the spanwise direction and $10h^*$ in the streamwise direction (Lozano-Durán & Jiménez 2014). Thus, the sizes of the computational domains are large enough to capture VLSMs and relatively smaller scale motions.

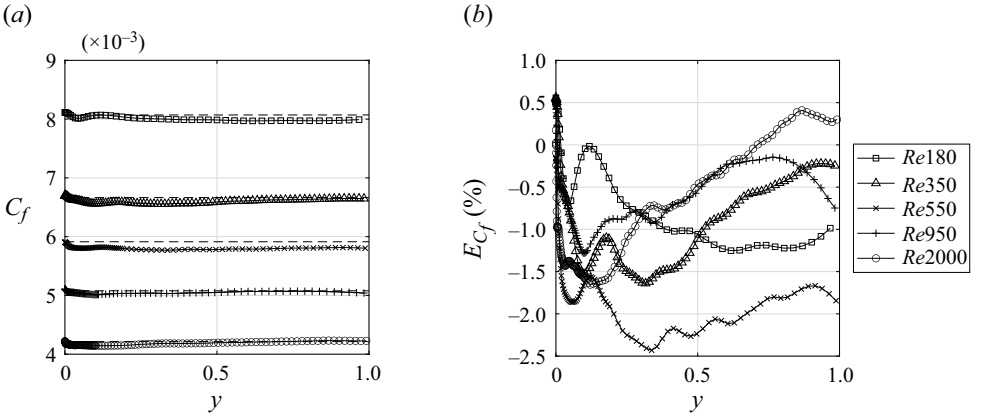

Figure 1. (*a*) Profiles of C_f estimated by (2.4) and $C_{f,ref}$ (nearest dashed lines) directly calculated by $C_{f,ref} = 2Re_\tau^2/Re_b^2$. (*b*) Relative errors between C_f and $C_{f,ref}$.

4. Results and discussion

Detailed descriptions and interpretations of the results are presented in this section. Profiles of C_{f1} and C_{f2} and their proportions based on (2.4) are given in § 4.1. Section 4.2 provides the spanwise co-spectra of velocity–vorticity correlations and corresponding scale-dependence of the contributing terms at different Reynolds numbers. Section 4.3 describes the quadrant decomposition of the velocity–vorticity correlations and their relations with the skin-friction drag generation.

4.1. *Statistics of the decomposition*

Figure 1(*a*) shows the variation of C_f calculated by (2.4) as a function of y, compared with the reference ones directly calculated by $C_{f,ref} = \langle\tau_w^*\rangle/(\frac{1}{2}\rho^* u_b^{*2}) = 2Re_\tau^2/Re_b^2$. Theoretically, the C_f calculated by (2.4) should remain constant regardless of the wall-normal location and match its reference value. Figure 1(*b*) shows the relative errors between C_f and $C_{f,ref}$, $E_{C_f}(y) = [C_f(y) - C_{f,ref}]/C_{f,ref}$. It can be seen that the errors are limited within $-2.5\,\% \le E_{C_f} \le 1\,\%$. Overall, the relative errors are acceptable, which validates the skin-friction drag decomposition method in (2.4) and lays the foundation for the further discussions.

Figure 2 shows the proportion profiles of the terms in (2.4) as a function of y^+ for the *Re*950 case. Similar trends are observed in other cases and not shown here for the sake of simplicity. Here, C_{f3} dominates the contributions in the viscous sublayer and decreases rapidly away from the wall. It is quite natural since C_{f3} equals to the non-dimensional mean streamwise shear stress $\langle\tau^*\rangle(y)/(\frac{1}{2}\rho^* u_b^{*2})$, which goes to C_f when $y \to 0$ and descends fast when y goes out of the near-wall region. Furthermore, C_{f4} is mathematically equal to yC_f, so its proportion scales up from 0 to 100 % and exhibits an exponential curve in the single logarithmic coordinate. Regarding C_{f1} and C_{f2}, the primary focuses in this study, we will present their specific trends and Reynolds number effects in the following.

Figure 3 illustrates the value profiles of C_{f1} and C_{f2} as a function of inner scale y^+. In figure 3(*a*), C_{f1} holds negative values for all cases at most wall-normal distances except for the near-wall region where there appears a merely positive peak. Figure 3(*b*) reveals that C_{f2} is totally positive. It seems that at $y = 1$, either C_{f1} or C_{f2} at all Reynolds numbers

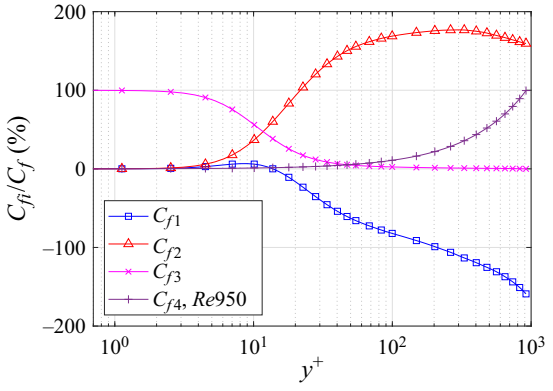

Figure 2. Proportion profiles of the contributing terms in (2.4) for case $Re950$.

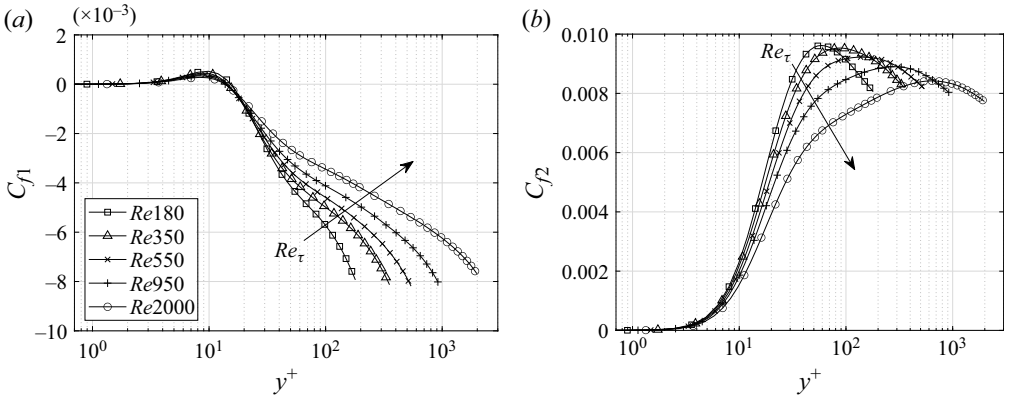

Figure 3. Value profiles of (*a*) C_{f1} and (*b*) C_{f2} versus y^+.

converge to an approximately constant value, but opposite, i.e. -0.008 for C_{f1} and 0.008 for C_{f2}. According to (2.2), we have $C_{f1} + C_{f2} = 2\langle -u'v'\rangle$ and $\langle -u'v'\rangle = 0$ at $y = 1$, so it is a direct consequence that the converged value of C_{f1} equals to that of $-C_{f2}$. The nearly constant converged value for all cases may indicate that the accumulated intensities, to some extent, are not sensitive to Reynolds numbers (at least for the five cases considered in this study).

Moreover, both C_{f1} and C_{f2} exhibit more gentle slopes at higher Re_τ, which indicates that the integrands of C_{f1} and C_{f2}, i.e. the velocity–vorticity correlations, tend to be less intense at higher Re_τ, as shown in figure 4. Integration of each curve returns to the corresponding individual skin-friction drag coefficient term. Profiles of all cases reach local peaks at the same wall-normal distance, and the peak values are inclined to be smaller at higher Reynolds numbers. Tennekes & Lumley (1972) stated that $\langle v\omega_z\rangle$ and $\langle -w\omega_y\rangle$ are body forces in the streamwise direction associated with transport and stretching of vorticity, respectively. This was in tune with another understanding that they are the streamwise component of the Lamb vector. As shown in figure 4(*a*), the negative $\langle v\omega_z\rangle$ in most of the wall-normal distance apart from the near-wall region represents the streamwise deceleration arising from the vortex transport. The streamwise deceleration contributes negatively to the generation of skin friction. Meanwhile, the positive $\langle -w\omega_y\rangle$ (figure 4*b*) reflects the streamwise acceleration that contributes positively to the skin friction.

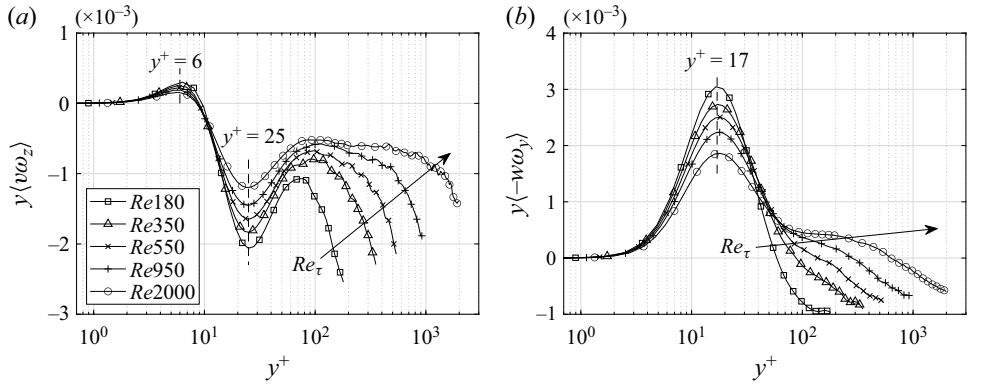

Figure 4. Profiles of (*a*) $y\langle v\omega_z\rangle$ and (*b*) $y\langle -w\omega_y\rangle$ versus y^+.

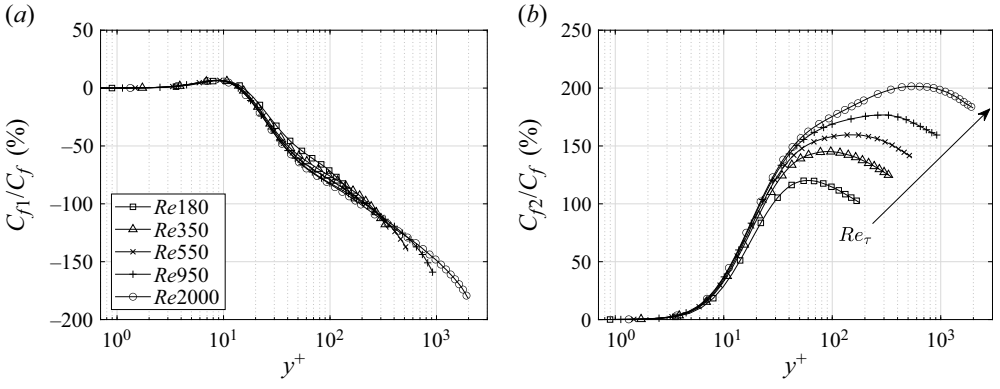

Figure 5. Proportion profiles of (*a*) C_{f1}/C_f and (*b*) C_{f2}/C_f versus y^+.

This coheres with the four-layer model of the dynamical and vortical processes proposed by Klewicki (2013), in which the stretching vortices were surmised to act as a momentum source in the inner region and the advecting vortices as the momentum sink above the inner region. Although the positive value concentrates in the region where $y < 0.3$ (not marked in this figure) for all Reynolds numbers, it makes the decisive contribution on the overall positive C_{f2}. In other words, the streamwise acceleration below $y = 0.3$ caused by the vortex stretching is the critical factor contributing to the skin friction.

Figure 5 shows the proportions of C_{f1} and C_{f2} to C_f, which measure their relative contributions. In figure 5(*a*), a plausible collapse emerges among curves of C_{f1}/C_f versus y^+. The values at $y = 1$ decrease with Re_τ, owing to the nearly constant C_{f1} there and the descent of C_f with the increase of Re_τ. A similar trend of C_{f2}/C_f at $y = 1$ is observed in figure 5(*b*). Higher proportion at high Re_τ suggests relatively more active vortical contributions of C_{f1} and C_{f2}.

Moreover, end points in figure 5(*b*) appear to be aligned on the semi-logarithmic coordinate, then a natural inference is that $1/C_f$ may be linearly related to $\lg Re_\tau$. Figure 6(*a*) presents the value of $1/C_f$ versus Re_τ in log scale. A well-fitted relation is obtained as

$$C_f = \frac{1}{110.62\lg Re_\tau - 130.63}. \tag{4.1}$$

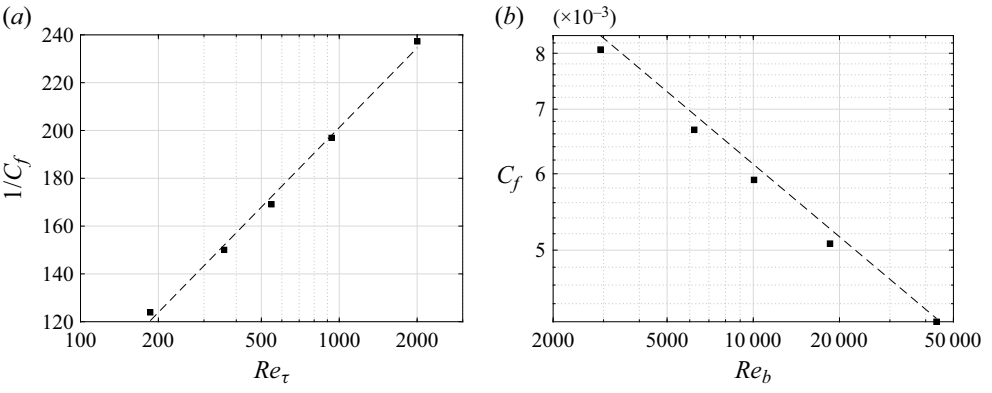

Figure 6. Variation of C_f as a function of (*a*) Re_τ and (*b*) Re_b. (■) Actual computed value for each case. (*a*) Fitted line (– –) by the five cases; (*b*) reference line (– –) of Dean (1978), $C_f = 0.073 \times (2Re_b)^{-0.25}$.

The R-squared value is 0.9955, suggesting a good fitting effect. Another classic prediction of C_f as a function of Re_b (Dean 1978), $C_f = 0.073 \times (2Re_b)^{-0.25}$, is also plotted in figure 6(*b*), with the R-squared value being 0.9752, slightly lower than that of the fitted line (4.1).

4.2. *Pre-multiplied spanwise co-spectra and positive/negative structure contributions*

As the Reynolds number increases, the inner and outer scale separation becomes more profound in wall-bounded turbulent flows (Jiménez 2018). The scale separation is associated with the population of energy-containing eddies in the logarithmic region (Lozano-Durán, Bae & Encinar 2020), and the generation of LSMs and VLSMs in the logarithmic and outer region (Del Álamo *et al.* 2004; Hutchins & Marusic 2007; Sillero, Jiménez & Moser 2013). The LSMs and VLSMs exert footprints and modulations on the near-wall flow quantities and further on the skin-friction drag. Therefore, extracting large-scale motions is significant to investigate the generation mechanism of skin-friction drag.

To divide the small- and large-scale structures with the low-pass spatial filtering, an appropriate cutoff wavelength needs to be determined. Actually, there was no strict standard for selecting the cutoff wavelength. The criterion $\lambda_z^* = \alpha h^*$ is widely adopted to investigate the velocity structures, where α is a parameter of order $O(1)$ selected differently in previous studies (Hutchins & Marusic 2007; Lee & Moser 2019; Doohan, Willis & Hwang 2021). With respect to the co-spectra of velocity–vorticity correlations, coupling the dynamics of velocity and vorticity structures, the low-pass filter with this cutoff wavelength fails to properly extract the small- and large-scale motions, see Appendix E.

Here, we attempt to use an alternative filtering criterion to separate the scales of velocity–vorticity correlations based on the spanwise pre-multiplied co-spectra of the turbulent inertia, $yk_z\phi_{TI}$. Figure 7 displays $yk_z\phi_{TI}$ for all cases, where $k_z = 2\pi/\lambda_z$ is the spanwise wavenumber, λ_z is the spanwise wavelength and ϕ_{TI} is the spanwise co-spectra calculated by $\phi_{TI} = \partial \mathrm{Re}(-\widehat{\overline{u'}}\widehat{v'})/\partial y$. The variables with a hat represent their Fourier transform, the complex number with an overbar represents its conjugate and Re means taking the real part. Chin *et al.* (2014) studied the streamwise co-spectra of the turbulent inertia and separated the large-/small-scale motions by streamwise scale. However, if the

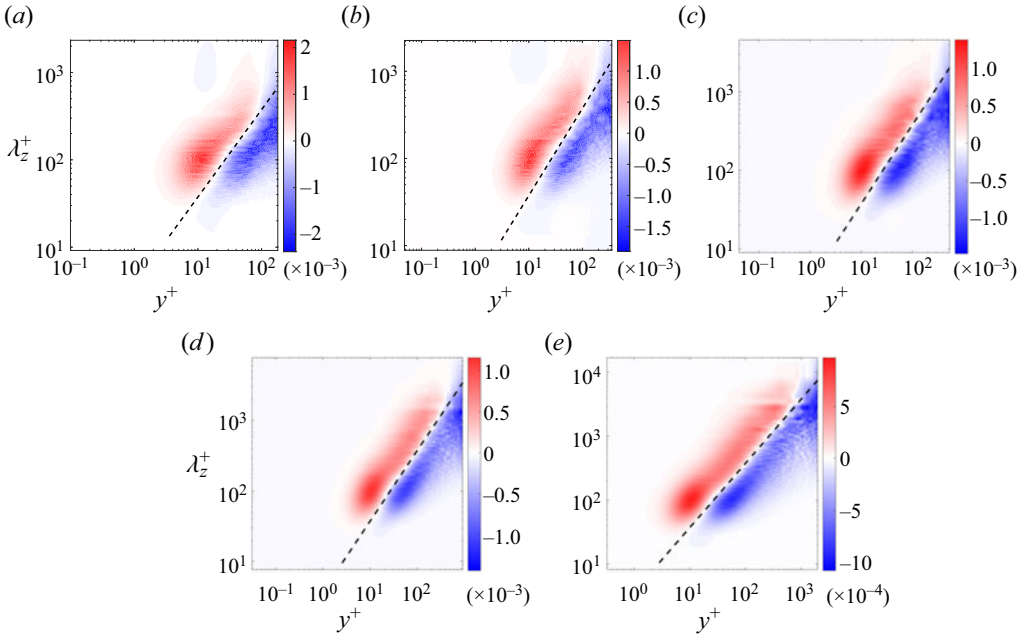

Figure 7. Spanwise pre-multiplied co-spectra of the turbulent inertia $yk_z\phi_{TI}$ for increasing Reynolds number in panels (*a–e*). The dashed line indicates $\lambda_z^+ = 3.75y^+$.

streamwise Fourier mode is used, it is difficult to distinguish the inter-scale energy transfer (like the scale interaction) from the intra-scale one (like the self-sustaining process). The spanwise Fourier mode could avoid this problem (Hwang 2015; Cho, Hwang & Choi 2018), so we use the spanwise co-spectra instead of the streamwise ones here.

In figure 7, it is interesting to find that the spectral space is clearly divided into two individual negative and positive regions, with a linear relationship of $\lambda_z^+ = 3.75y^+$ (the dashed lines). The positive and negative regions also appear to be scaled linearly with distance from the wall. These features do not vary with Reynolds number, and the linear relationship of $\lambda_z^+ = 3.75y^+$ seems to be universal and not sensitive to the Reynolds number.

To analyse the connection between the turbulent inertia and Reynolds stress, we show their co-spectra, i.e. $yk_z\phi_{TI}$ and $k_z\phi_{-u'v'}$, in figure 8 for case *Re*2000. By definition, $yk_z\phi_{TI}$ is the wall-normal gradient of $k_z\phi_{-u'v'}$ (with a logarithmic scale in y^+). Therefore, the positive region in $yk_z\phi_{TI}$ means that the Reynolds stress at the given spanwise scale is amplified in the wall-normal direction, and *vice versa*. The dividing line $\lambda_z^+ = 3.75y^+$ in $yk_z\phi_{TI}$ corresponds to the ridge line in $k_z\phi_{-u'v'}$, indicating the linear spanwise scale growth of the Reynolds stress with the distance from the wall.

In the study of De Giovanetti, Hwang & Choi (2016), three energy-containing motions were clearly identified from the Reynolds stress co-spectra. (i) The motions at $\lambda_z^+ \approx 100$ are composed of the near-wall streaks and the quasi-streamwise vortices. The inner positive and negative peaks of the TI co-spectra are also at the scale $\lambda_z^+ \approx 100$. (ii) The motions at the outer length scale $\lambda_z \approx 1.5$ are represented by the VLSMs (outer streaks) and the LSMs (outer streamwise vortical structures). (iii) At the log-layer length scale between $\lambda_z^+ \approx 100$ and $\lambda_z \approx 1.5$, the motions with λ_z growing linearly with y are self-similar to one another, in accordance with the attached eddy hypothesis proposed by Townsend (1976). These features can also be identified in the TI co-spectra. The scales

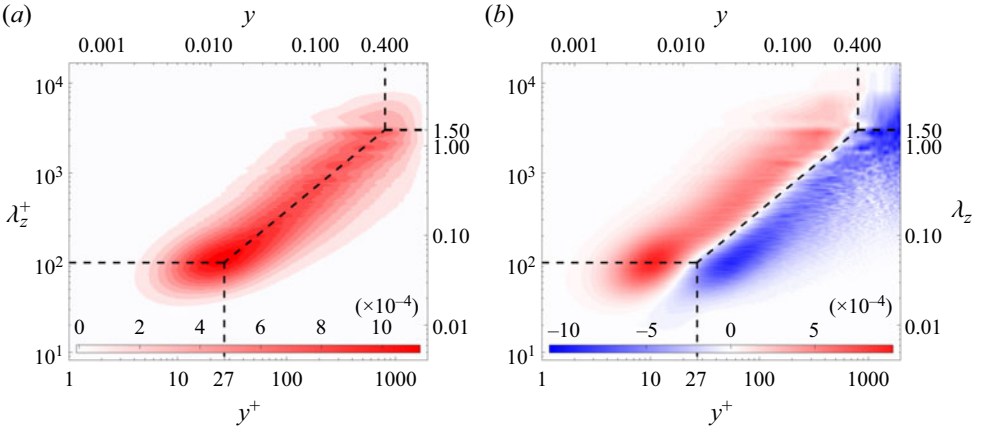

Figure 8. Spanwise pre-multiplied co-spectra of (*a*) the Reynolds stress $k_z\phi_{-u'v'}$ and (*b*) the turbulent inertia $yk_z\phi_{TI}$ for case *Re*2000. The dashed diagonal indicates $\lambda_z^+ = 3.75y^+$.

of the energy-containing motions are universal at different Reynolds numbers, thus not shown for brevity.

Considering that $\lambda_z^+ = 3.75y^+$ is not sensitive to the Reynolds number and the turbulent inertia combines the dynamics of velocity–vorticity correlations (see (1.3)), we employ $\lambda_z^+ = 3.75y^+$ as the filtering criterion to extract the structures associated with the positive and negative contributions to the skin-friction drag generation. A similar criterion with a varying cutoff wavelength is also applied by Chan, Schlatter & Chin (2021) to distinguish the large- and small-scale components of inter-scale transport of Reynolds shear stress. In this work, we address these two separated regions as positive structures (PSs) and negative structures (NSs), and they also imply the local large- and small-scale structures, respectively. Since the turbulent inertia indicates the streamwise body force, it could be inferred that the PSs lead to the streamwise acceleration and the NSs are associated with the streamwise retardation.

Recall from (2.2), the spanwise pre-multiplied co-spectra of the turbulent inertia can also be decomposed into that of $v\omega_z$ and $-w\omega_y$, i.e. $yk_z\phi_{v\omega_z}$ and $yk_z\phi_{-w\omega_y}$, which are displayed in figure 9 for the cases of *Re*180, *Re*950 and *Re*2000. Similar features are observed in the other two cases, but not shown here for brevity. We find that $yk_z\phi_{v\omega_z}$ is dominated by negative values, with a peak at $y^+ = 10$–30 and $\lambda_z^+ = 100$, regardless of the Reynolds numbers. The peak of $yk_z\phi_{-w\omega_y}$ locates at the same wall-normal position and spanwise wavelength as $yk_z\phi_{v\omega_z}$, but with opposite sign. The filtering criterion $\lambda_z^+ = 3.75y^+$ is plotted in figure 9 as dashed lines. Several noticeable features can be observed by using this varying cutoff wavelength: (i) in terms of $yk_z\phi_{v\omega_z}$, the cutoff line roughly goes through the negative peak and a spoon-handle-shaped extension of negative motions in the outer region distributes along this line; (ii) two weak positive areas are assigned in PSs as well as a negative part populated at $y^+ = 10$–50 (which presents a bit of an extension towards local larger scale); (iii) negative part of $yk_z\phi_{-w\omega_y}$ is assigned in NSs, while motions in PSs contribute positively to skin-friction drag apart from a negative part in the outer region above the line. The dominant negative $yk_z\phi_{v\omega_z}$ and positive $yk_z\phi_{-w\omega_y}$ also support the four-layer model given by Klewicki (2013).

Priyadarshana *et al.* (2007) stated that the co-spectra of velocity–vorticity correlations tend to gain peaks at wavelengths near the peaks of individual components (velocity and

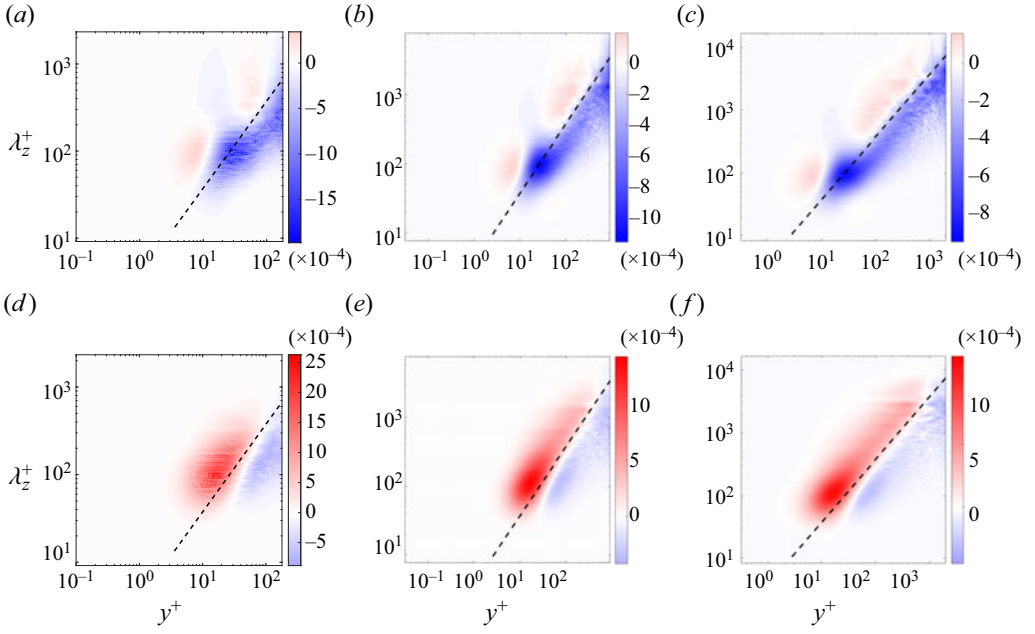

Figure 9. Pre-multiplied spanwise co-spectra (*a–c*) $yk_z\phi_{v\omega_z}$ and (*d–f*) $yk_z\phi_{-w\omega_y}$. (*a,d*) *Re*180; (*b,e*) *Re*950; (*c,f*) *Re*2000. The dashed line indicates $\lambda_z^+ = 3.75y^+$.

vorticity itself) at a fixed wall-normal distance. According to this, we can interpret the attribution of the inner peak and outer extension of velocity–vorticity co-spectra. On one hand, the inner peak of the co-spectra with approximately constant position and length scale at different Reynolds numbers, as displayed in figure 9, is probably related to the vorticity component, since vortical motions approximately maintain a relatively small scale as Reynolds number increases. On the other hand, as Reynolds number increases, the co-spectra extend to the outer region with considerable energy. This may be attributed to the velocity structures, in terms of LSMs and VLSMs populating in the outer region, especially at high Reynolds numbers.

At a fixed y^+, $\langle v\omega_z\rangle$ and $\langle -w\omega_y\rangle$ of PSs and NSs can be obtained by integrating the respective co-spectra along $\lambda_z^+ > 3.75y^+$ and $\lambda_z^+ < 3.75y^+$. Their profiles multiplied by y are shown in figure 10. Two positive peaks of $y\langle v\omega_z\rangle_{PS}$ in figure 10(*a*) are associated with the two weak positive areas in the near-wall and logarithmic region, respectively; whereas the intense minimum at $y^+ \approx 20$ is related to the extension of local negative events towards larger scale, see figures 9(*a*)–9(*c*). In figure 10(*b*), $y\langle v\omega_z\rangle_{NS}$ stays negative now that the positive areas are all assigned in PSs, and the local minimum at $y^+ = 42$ is relevant to the negative peak of $yk_z\phi_{v\omega_z}$. Likewise, the positions of the maximum in figures 10(*c*) and 10(*d*) are also associated with the local inner peaks of $yk_z\phi_{-w\omega_y}$, and almost positive values in figure 10(*c*) correspond to aforementioned feature (iii). Each curve reaches the maximum or minimum at a constant wall-normal position in the near-wall region in figure 10, indicating that the structures are well scaled by inner units. Additionally, profiles in figures 10(*b*) and 10(*d*) at higher Reynolds number appear to form plateaus in part of the logarithmic region (referenced by the red dashed line), implying that $\langle v\omega_z\rangle_{NS}$ and $\langle -w\omega_y\rangle_{NS}$ are inversely proportional to the wall-normal distance.

Overall, it is clear that lower Reynolds number leads to a greater absolute value in inner peaks and outer region (versus y, not shown here). As mentioned in § 4.1,

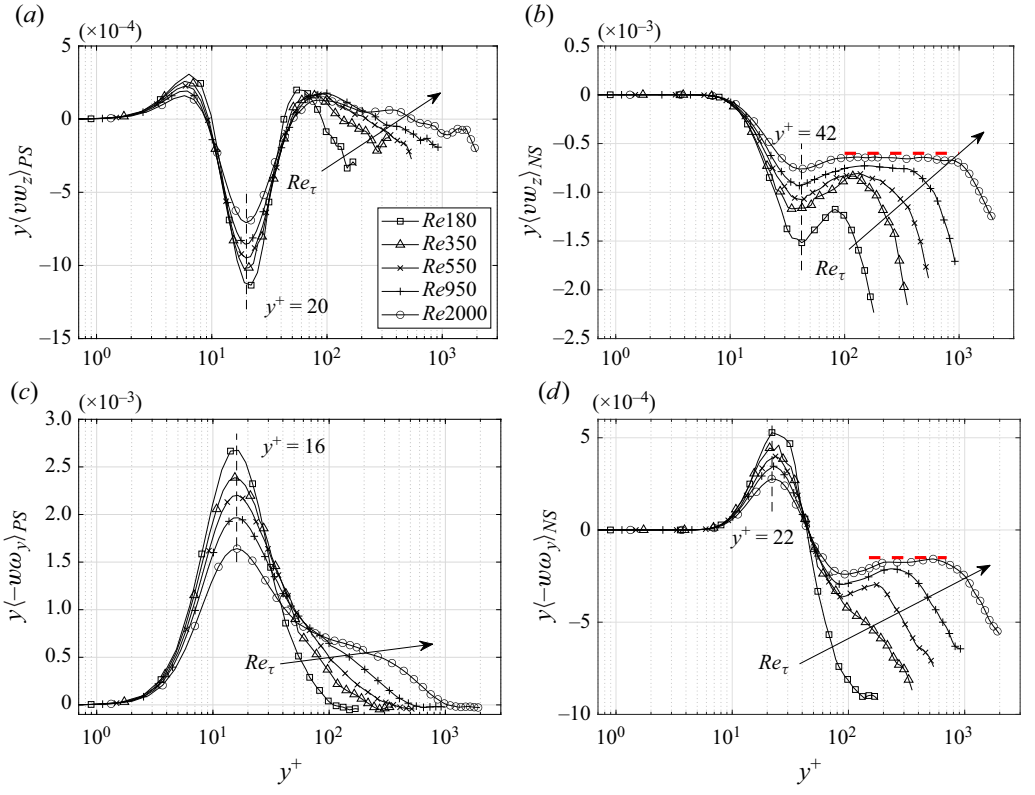

Figure 10. Profiles of (*a*) $y\langle v\omega_z\rangle_{PS}$, (*b*) $y\langle v\omega_z\rangle_{NS}$, (*c*) $y\langle -w\omega_y\rangle_{PS}$ and (*d*) $y\langle -w\omega_y\rangle_{NS}$ versus y^+. Red dashed line in panels (*b*) and (*d*) is a reference line for plateaus.

C_{f1} and C_{f2} converge to the approximately same respective value for all cases, which means double integrals of the pre-multiplied co-spectra $yk_z\phi_{v\omega_z}$ (figures 9*a*–9*c*) and $yk_z\phi_{-w\omega_y}$ (figures 9*d*–9*f*) on the full plane are respectively equal. Nevertheless, with Reynolds number increasing, more larger-scale motions, whether positive or negative, occur and manifest as the extension in the logarithm region, taking up a certain proportion and hence draining peaks in the inner and outer region.

Regarding C_{f1} and C_{f2}, they can be further divided into two parts by integrating the velocity–vorticity correlations in PSs and NSs, *viz.*,

$$C_{f1}^{PS}(y^+) = \int_0^{y^+}\int_{\lambda_z^+>3.75y^+} yk_z\phi_{v\omega_z}\,\mathrm{d}\ln\lambda_z^+\mathrm{d}\ln y^+, \tag{4.2a}$$

$$C_{f1}^{NS}(y^+) = \int_0^{y^+}\int_{\lambda_z^+<3.75y^+} yk_z\phi_{v\omega_z}\,\mathrm{d}\ln\lambda_z^+\mathrm{d}\ln y^+, \tag{4.2b}$$

$$C_{f2}^{PS}(y^+) = \int_0^{y^+}\int_{\lambda_z^+>3.75y^+} yk_z\phi_{-w\omega_y}\,\mathrm{d}\ln\lambda_z^+\mathrm{d}\ln y^+, \tag{4.2c}$$

$$C_{f2}^{NS}(y^+) = \int_0^{y^+}\int_{\lambda_z^+<3.75y^+} yk_z\phi_{-w\omega_y}\,\mathrm{d}\ln\lambda_z^+\mathrm{d}\ln y^+. \tag{4.2d}$$

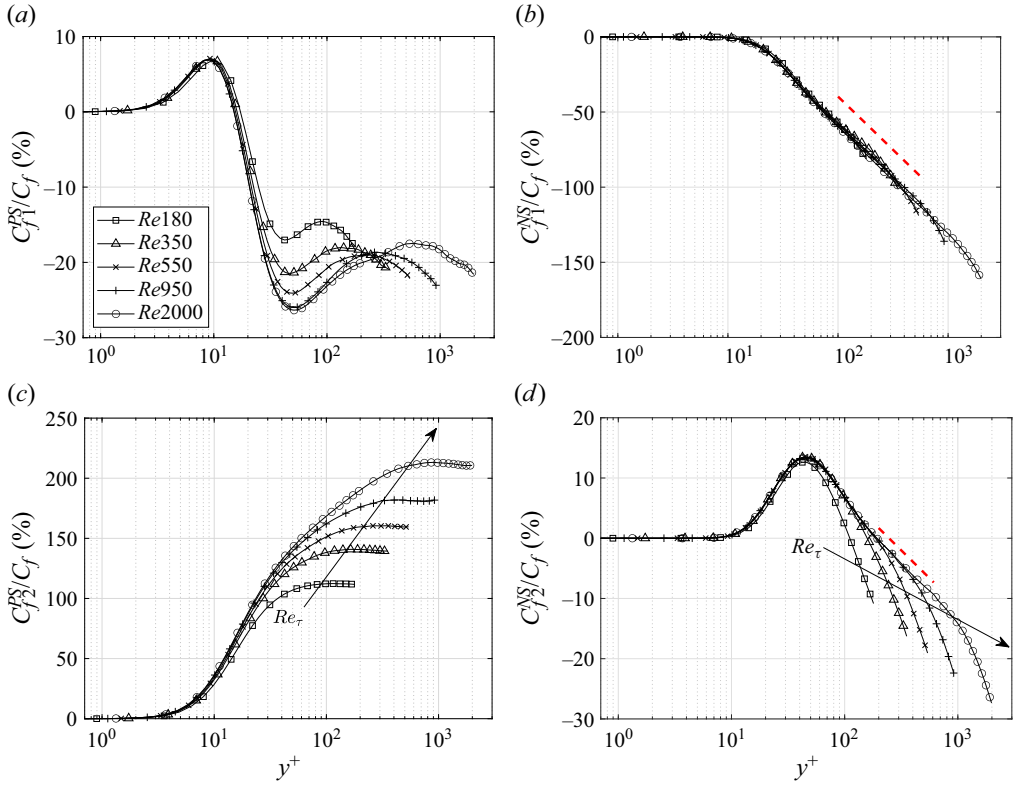

Figure 11. Proportion profiles of (*a*) C_{f1}^{PS}, (*b*) C_{f1}^{NS}, (*c*) C_{f2}^{PS} and (*d*) C_{f2}^{NS} in total C_f versus y^+. Red dashed line in panels (*b*) and (*d*) is a reference line for log-law.

Profiles of C_{fi}^{PS} and C_{fi}^{NS} $(i = 1, 2)$ can be found in Appendix F. Here, the contributions are divided by C_f to discuss the Reynolds number effects in the proportion of individual contribution. Figure 11 shows the profiles of C_{fi}^{PS}/C_f and C_{fi}^{NS}/C_f as a function of y^+.

As a consequence of the dominant position of C_{f1}^{NS} in C_{f1} and C_{f2}^{PS} in C_{f2}, proportion C_{f1}^{NS}/C_f and C_{f2}^{PS}/C_f collapse better with C_{f1}/C_f and C_{f2}/C_f, respectively. Compared with figure 5, figure 11(*b*) reveals less distinctions (which are caused by C_{f1}^{PS}) at different Reynolds numbers, which means that the contribution proportion of local small-scale advective vorticity transport on the skin friction is less influenced by Reynolds number in inner units. Moreover, a log-law occurs in the logarithmic region (referenced by the nearby red dashed line). However, according to the plateaus in figure 10(*b*), the better log-law only occurs at higher Reynolds number, and the worse fitting in lower Reynolds number is weakened by overlapped curves. An analogous log-law appears in C_{f2}/C_f (figure 11*d*) at higher Reynolds number.

In the inner region, compared with the distinction peaks of C_{fi}^{PS} and C_{fi}^{NS} $(i = 1, 2)$, especially C_{f1}^{PS} and C_{f2}^{NS} (see Appendix F), their proportions to C_f appear to collapse well, suggesting the insensitivity to Reynolds number. In the outer region, although almost all the four components in figure 11 occupy a higher proportion with the increase of Reynolds number, the total C_f presents an opposite trend, indicating that the local small-/large-scale advective vorticity transport and vortex stretching cancel each other out to a larger extent.

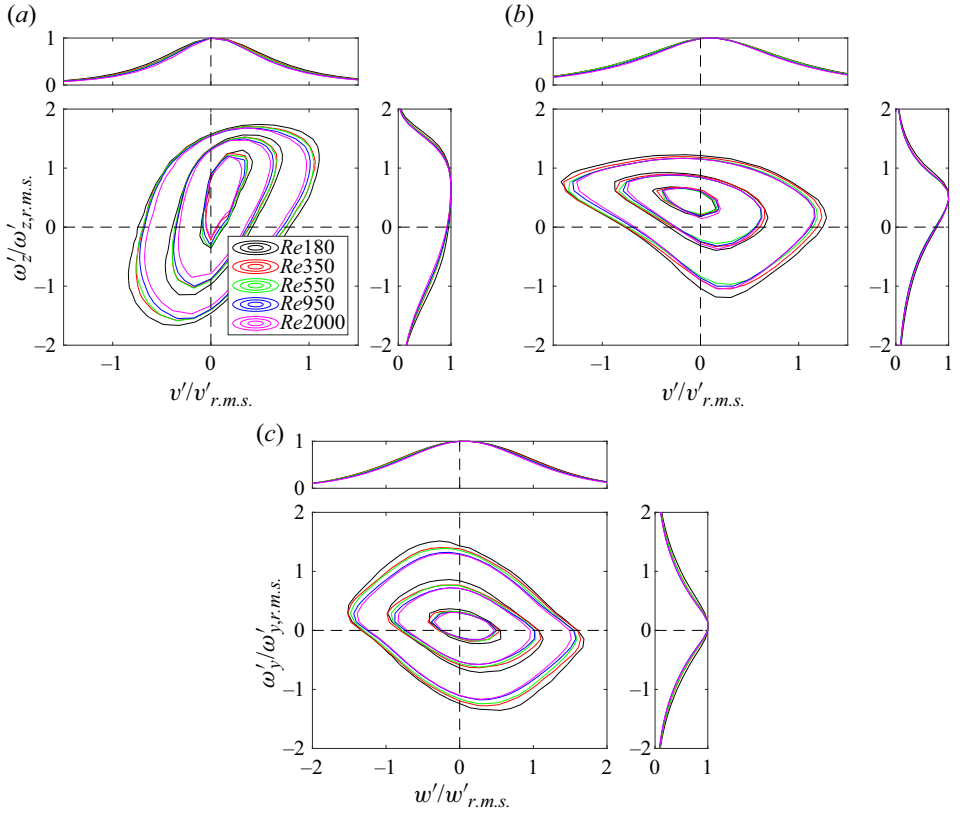

Figure 12. JPDFs normalized by each maximum of $v'\omega'_z$ at (*a*) $y^+ = 6$ and (*b*) $y^+ = 25$ and $w'\omega'_y$ at (*c*) $y^+ = 17$ with each axis normalized by its r.m.s. for all Reynolds numbers. Three clusters of contours in each panel represent 0.9, 0.6 and 0.3 from inside out. The top plot in each panel presents the marginal distributions (normalized by each maximum) of corresponding r.m.s.-normalized velocity fluctuation, and the right plot in each panel presents those of r.m.s.-normalized vorticity fluctuation.

4.3. *Quadrant analyses*

Quadrant decomposition of the velocity–vorticity correlations ($v'\omega'_z$ and $w'\omega'_y$) is performed to further investigate the friction drag generation linked to different quadrant motions. To provide a visual perspective of the quadrant motions, the joint probability distribution functions (JPDFs) of $v'\omega'_z$ and $w'\omega'_y$ are investigated at some wall-normal distances. Note that the components in the velocity–vorticity correlations are rewritten into corresponding fluctuations, the reason for which will be discussed later. We use the velocity component as the horizontal axis and vorticity component as the vertical axis to identify the quadrant.

Based on the peaks in figure 4, three typical locations at $y^+ = 6$, 17 and 25 are selected to check the JPDFs of $v'\omega'_z$ and $w'\omega'_y$, as displayed in figure 12. Figure 12(*a*) shows JPDFs of $v'\omega'_z$ at $y^+ = 6$ for all cases. The contour lines are normalized by each maximum value, and the axes are normalized by the root mean square (r.m.s.) of corresponding fluctuations. The normalized JPDFs contours have a nice collapse at different Reynolds numbers and are ellipse-like in shape whose major axes distribute along the first and third quadrants, leading to the JPDFs extension and dominantly distributing in these two quadrants (especially the first quadrant). Figure 12(*a*) reveals that the small positive $v'\omega'_z$ at $y^+ = 6$ is mainly

dominated by the upward anticlockwise-rotating motions ($v' > 0$ and $\omega_z' > 0$). A similar conclusion can be found by Chin *et al.* (2014), in which both JPDFs and weighted JPDFs (figures 6 and 7 in Chin *et al.* (2014)) were investigated to demonstrate this point. However, something wrong might exist in figure 6 of Chin *et al.* (2014), for instance, where the core of JPDF occurred at the third quadrant and the PDF of ω_z' was positively skewed. The sign of ω_z' is consistent with that of $-\partial u'/\partial y$ in the near-wall region, as $\omega_z' = \partial v'/\partial x - \partial u'/\partial y$. Generally, a positively skewed distribution of τ_w' is observed (e.g. Cheng *et al.* 2020), which suggests that the PDF of ω_z' is negatively skewed, as shown in the right panel of figure 12(*a*). The PDF of v' is also plotted in the top panel of figure 12(*a*), showing its relatively symmetric feature.

Figure 12(*b*) shows JPDFs of $v'\omega_z'$ at $y^+ = 25$. There exist the core and prominent extension in the second quadrant ($v' < 0$ & $\omega_z' > 0$) which is connected with the downward anticlockwise-rotating motions contributing to the negative peak of $v'\omega_z'$ most. Chin *et al.* (2014) pointed out that it could be viewed as the head of hairpin vortices advecting outwards, but this interpretation was based on the improper JPDF that the sign of the axes was opposite. The negative skewness of ω_z' is still obvious in the right plot, while the distribution of v' is relatively symmetric.

The JPDFs of $w'\omega_y'$ at $y^+ = 17$ are plotted in figure 12(*c*). Nice centre symmetry about the original point is observed. The dominant second and fourth quadrant motions are related to a couple of counter-rotating normal vortices who move oppositely in the spanwise direction. In addition, compared with ω_z', the distribution of $\omega_y'(= \partial u'/\partial z - \partial w'/\partial x)$ presents good symmetry owing to the homogeneity in the streamwise and spanwise directions.

Having investigated the schematic JPDFs of $v'\omega_z'$ and $w'\omega_y'$ at specific positions, we then focus on the quantitative intensity of $v'\omega_z'$ and $w'\omega_y'$ in each quadrant, i.e. $\langle v'\omega_z'\rangle_{Qi}$ and $\langle -w'\omega_y'\rangle_{Qi}$, where $i = 1$–4 and $\langle\varphi\rangle_{Qi} = \sum_j \varphi_j|_{\varphi_j\in Qi}/N$ (N is total mesh number at each height). The benefit of this definition of quadrant ensemble average rather than divided by $N|_{\varphi_j\in Qi}$ is to ensure $\langle\varphi\rangle = \sum_i\langle\varphi\rangle_{Qi}$. The reason why we adopt the velocity–vorticity correlations with fluctuation components is that the quadrant analyses are based on the concept of joint distribution of fluctuations and $\langle v\omega_z\rangle_{Qi} \neq \langle v'\omega_z'\rangle_{Qi}$ on account of $\bar{\omega}_z \neq 0$. Corresponding C_{f1}^{Qi} and C_{f2}^{Qi} are defined as

$$C_{f1}^{Qi} = \int_0^y y\langle v'\omega_z'\rangle_{Qi}\,\mathrm{d}\ln y, \tag{4.3a}$$

$$C_{f2}^{Qi} = \int_0^y y\langle -w'\omega_y'\rangle_{Qi}\,\mathrm{d}\ln y. \tag{4.3b}$$

Figure 13 shows the profiles of $\langle v'\omega_z'\rangle_{Qi}$ and $\langle -w'\omega_y'\rangle_{Qi}$ multiplied by y for case $Re950$. The results of other cases are not shown here because of high resemblance. All pre-multiplied $\langle v'\omega_z'\rangle_{Qi}$ (figure 13*a*) reach a mutual inhibition and consequently, by contrast, pre-multiplied $\langle v'\omega_z'\rangle$ is of relatively small amplitude above the inner region, where $v'\omega_z'$ in $Q2$ and $Q4$ (especially $Q4$) seems to be slightly in the lead compared with $Q3$ and $Q1$, promoting C_{f1} to be negative. Here, $Q2$ and $Q4$ correspond to downward anticlockwise-rotating motions and upward clockwise-rotating motions, respectively, with the latter inhibiting skin-friction drag most.

In terms of $\langle -w'\omega_y'\rangle_{Qi}$ (figure 13*b*), it is obvious that $\langle -w'\omega_y'\rangle_{Q2}$ and $\langle -w'\omega_y'\rangle_{Q4}$ collapse perfectly, and so do $\langle -w'\omega_y'\rangle_{Q1}$ and $\langle -w'\omega_y'\rangle_{Q3}$. This collapse is due to the symmetry of the value distribution of w' and ω_y', as shown in the top and right plots of

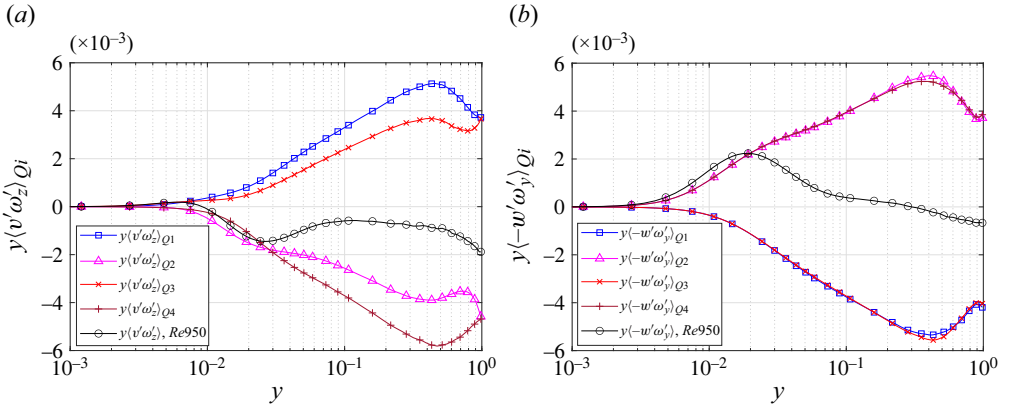

Figure 13. Profiles of (*a*) $y\langle v'\omega'_z\rangle_{Qi}$ and (*b*) $y\langle -w'\omega'_y\rangle_{Qi}$ ($i = 1 - 4$) versus y for case $Re950$.

figure 12(*c*), and this symmetry holds throughout the whole channel height. Here, C_{f2}^{Qi} is the integral of $\langle -w'\omega'_y\rangle_{Qi}$, and accordingly, it collapses perfectly as well, which is not observed in C_{f1} on account of the asymmetry of ω'_z. Additionally, despite symmetry of w' and ω'_y, they are not necessarily independent and their joint distributions exhibit a central symmetry but not necessarily a uniform symmetry. That is to say, $Q2$ and $Q4$ distribute necessarily symmetrically, and so do $Q1$ and $Q3$, but $Q1$ and $Q2$ are not necessarily symmetric. For example, there is a degree of skewness where $Q2$ and $Q4$ are a bit more intense than $Q1$ and $Q3$ in the region where $y < 0.3$, leading to the positive $\langle -w'\omega'_y\rangle$, especially in the near-wall region (as shown in figure 12*c*). The skewness is approximately negligible in the vicinity of the zero point ($y = 0.3$) of $\langle -w'\omega'_y\rangle$ and the JPDF is relatively uniform there.

Profiles of pre-multiplied $\langle v'\omega'_z\rangle_{Qi}$ and $\langle -w'\omega'_y\rangle_{Qi}$ as well as corresponding proportion of C_{f1}^{Qi} and C_{f2}^{Qi} to C_f are shown for all Reynolds numbers in figure 14. By reason of the symmetry of the distributions of w' and ω'_y mentioned above, profiles of $\langle -w'\omega'_y\rangle_{Qi}$ gain excellent collapse in diagonal quadrants as shown in figures 14(*b*-i,*b*-iii), 14(*b*-ii,*b*-iv), 14(*d*-i,*d*-iii) and 14(*d*-ii,*d*-iv). This is not remarkable in $v'\omega'_z$. Additionally, it is obvious that all quantities are amplified with the increase of Reynolds number (see figure 14*a*,*b*), of which the root cause is that the high Reynolds number excites more intense fluctuations, thus $\langle v'\omega'_z\rangle_{Qi}$ and $\langle -w'\omega'_y\rangle_{Qi}$ could reach larger values. Furthermore, the proportion profiles of C_{f1}^{Qi} and C_{f2}^{Qi} follow the same rule (see figure 14*c*,*d*).

It seems that all pre-multiplied quadrant velocity–vorticity correlations in figure 14 reach the extreme value at the position around $y = 0.48$ at all Reynolds numbers, suggesting that near this position, all quadrant motions are scaled with the outer units and approximately contribute most to the skin-friction drag, but as shown in figure 13, all quadrant motions reach a balance here and consequently no prominent feature occurs for the total pre-multiplied correlations at this position. In addition, according to figure 3, total C_{f1} and C_{f2} converge to the same respective value at $y = 1$ for all cases, indicating that amplifications of quadrant quantities at higher Reynolds number almost cancel each other out in the vicinity of the central plane. Figure 15 displays C_{f1}^{Qi} and C_{f2}^{Qi} ($i = 1 - 4$) at $y = 1$ for all cases. Each profile exhibits the approximately linear growth as the increase of Reynolds number. Because of the nearly constant convergent value of C_{f1} and C_{f2}, the summation of all profiles in each of figures 15(*a*) and 15(*b*) is constant.

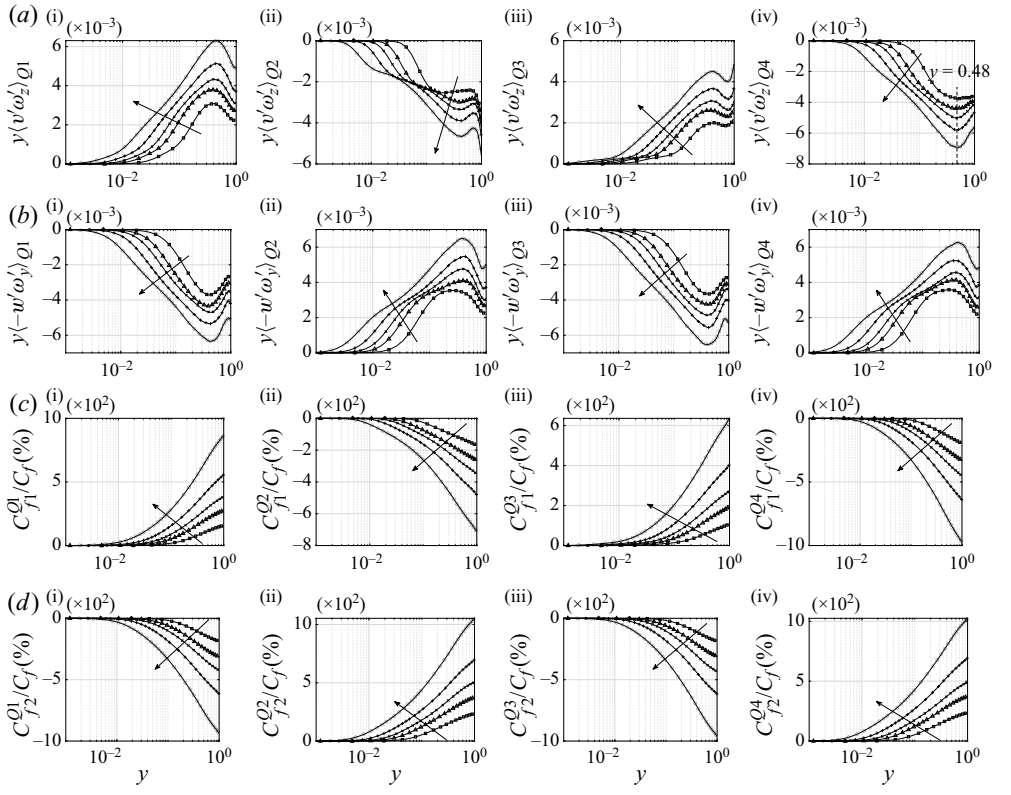

Figure 14. Profiles of (*a*-i) $y\langle v'\omega'_z\rangle_{Qi}$, (*b*-i) $y\langle -w'\omega'_y\rangle_{Qi}$, (*c*-i) C_{f1}^{Qi}/C_f and (*d*-i) C_{f2}^{Qi}/C_f $(i = 1-4)$ versus y for all five cases: (□) *Re*180, (△) *Re*350, (×) *Re*550, (+) *Re*950, (○) *Re*2000. Arrows represent that the Reynolds number increases.

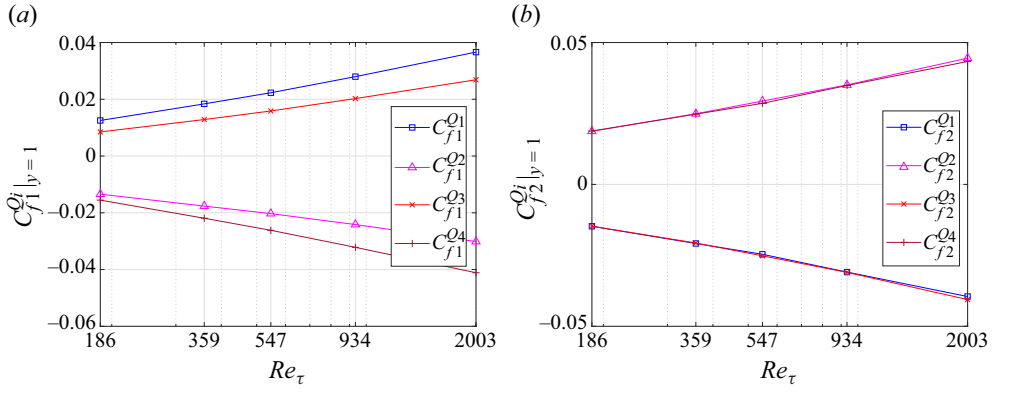

Figure 15. Profiles of (*a*) C_{f1}^{Qi} and (*b*) C_{f2}^{Qi} $(i = 1-4)$ at $y = 1$ versus Re_τ.

5. Concluding remarks

In the present study, we have given a form of skin-friction drag decomposition (2.4) based on the velocity–vorticity correlations. Better physics-informed interpretation could be inferred from this form since it does not suffer from the weight factor $(1 - y)$ appearing in other FIK-like identities. By using cases of incompressible turbulent channel flows at friction Reynolds numbers from 186 to 2003, we investigate the Reynolds number effects

on the contributing terms, their scale-dependence and quadrant characteristics. The key findings are summarized as follows.

(i) C_{f1}, which is generated from the advective vorticity transport ($v\omega_z$), contributes negatively to the skin friction except in the near-wall region; whereas C_{f2}, which is associated with the vortex stretching ($-w\omega_y$), is overall positive. The negative $\langle v\omega_z\rangle$ characterizes the streamwise deceleration (or the momentum sink) arising from the vortex transport. Reversely, the positive $\langle -w\omega_y\rangle$ reflects the streamwise acceleration (or the momentum source). The pre-multiplied intensities of $\langle v\omega_z\rangle$ and $\langle -w\omega_y\rangle$ reach peaks at positions that are independent on the Reynolds number, where they locally contribute most to C_{f1} and C_{f2}, respectively. At $y = 1$, either C_{f1} or C_{f2} converges to an approximately constant value regardless of the Reynolds number.

(ii) It is found that the spanwise pre-multiplied co-spectra of the turbulent inertia is clearly divided into individual positive and negative regions, with a universal linear relationship of $\lambda_z^+ = 3.75y^+$ for all cases. The scaling law could be observed in the co-spectra of both the Reynolds stress and the turbulent inertia, indicating the connection with the self-similar energy-containing motions predicted by the attached eddy hypothesis. We adopt this varying cutoff wavelength as a scale separation strategy, to decompose the turbulent motions into positive (PSs) and negative (NSs) structures. Results show that the advective vorticity transport is principally responsible for NSs acting as the momentum sink, while the vortex stretching is the main cause of PSs acting as the momentum source. From another perspective, NSs and PSs also represent the local small- and large-scale motions, respectively, suggesting that the advective vorticity transport is statistically in smaller scale, while the vortex stretching process is quite the contrary. Consequently, NSs and PSs play the dominant role in the generation of C_{f1} and C_{f2}, respectively. Extreme points of pre-multiplied $\langle v\omega_z\rangle$ and $\langle -w\omega_y\rangle$ of PSs and NSs are connected with peaks in the corresponding spanwise pre-multiplied co-spectra in the inner region and consistent at different Reynolds numbers. Moreover, a log-law occurs in profiles of C_{f1}^{NS} and C_{f2}^{NS} in the logarithmic region only at high Reynolds numbers.

(iii) The joint probability distribution functions (JPDFs) of the velocity–vorticity correlations ($v'\omega_z'$ and $w'\omega_y'$) in the inner region exhibit skewness in the quadrants, which is directly linked to the inner peaks of correlations. The second and fourth quadrant motions of $w'\omega_y'$ are dominant at $y^+ = 17$, which is related to the generation mechanism of vortex stretching. As the wall-normal distance increases, JPDFs tend to be more uniform, especially for $w'\omega_y'$. Additionally, $\langle v'\omega_z'\rangle_{Qi}$ and $\langle -w'\omega_y'\rangle_{Qi}$ are enhanced with the increase of Reynolds number by reason that the high Reynolds number excites more intense fluctuations. Nevertheless, intensities of all quadrants reach a mutual inhibition and consequently their summations vary in relatively small amplitudes. Their integrals, i.e. C_{f1}^{Qi} and C_{f2}^{Qi}, and proportions to C_f also share the same conclusion.

Acknowledgements. Special thanks to Dr C. Cheng at The Hong Kong University of Science and Technology for his utmost assistance.

Funding. The funding support of the National Natural Science Foundation of China (under the grant nos. 12372221 and 92052101) is acknowledged.

Declaration of interests. The authors report no conflict of interest.

Author ORCIDs.
Yitong Fan https://orcid.org/0000-0001-8583-9670;
Weipeng Li https://orcid.org/0000-0002-0335-4934.

Appendix A. Reduce Yoon's identity to the FIK identity

One can perform a fourfold integration $\int_0^1 \int_0^y \int_0^{y_3} \int_0^{y_2} \mathrm{d}y_1\,\mathrm{d}y_2\,\mathrm{d}y_3\,\mathrm{d}y$ (where y, y_1, y_2 and y_3 are all wall-normal distances) to the mean spanwise vorticity equation, to reduce Yoon's identity to the FIK identity. We give a brief proof here.

The mean spanwise vorticity equation is expressed as

$$\frac{\mathrm{d}\langle v\omega_z\rangle}{\mathrm{d}y} + \frac{\mathrm{d}\langle -w\omega_y\rangle}{\mathrm{d}y} - \frac{1}{Re_b}\frac{\mathrm{d}^2\langle\omega_z\rangle}{\mathrm{d}y^2} = 0. \tag{A1}$$

Performing the first integration $\int_0^{y_2} \mathrm{d}y_1$ to (A1), we obtain

$$\langle v\omega_z\rangle + \langle -w\omega_y\rangle - \frac{1}{Re_b}\frac{\mathrm{d}\langle\omega_z\rangle}{\mathrm{d}y} + \frac{1}{Re_b}\frac{\mathrm{d}\langle\omega_z\rangle}{\mathrm{d}y}\bigg|_{y=0} = 0. \tag{A2}$$

Substituting the turbulent inertia decomposition (2.2) as well as $\langle\omega_z\rangle = -\mathrm{d}\langle u\rangle/\mathrm{d}y$ into (A2), we have

$$\frac{\mathrm{d}\langle -u'v'\rangle}{\mathrm{d}y} + \frac{1}{Re_b}\frac{\mathrm{d}^2\langle u\rangle}{\mathrm{d}y^2} + \frac{1}{Re_b}\frac{\mathrm{d}\langle\omega_z\rangle}{\mathrm{d}y}\bigg|_{y=0} = 0. \tag{A3}$$

Comparing (A3) with the equation of the streamwise mean momentum balance (2.1), we can find that $(\mathrm{d}\langle u\rangle/\mathrm{d}y)|_{y=0} = (\mathrm{d}\langle\omega_z\rangle/\mathrm{d}y)|_{y=0}$. This indicates that (A3) (i.e. the integral of (A1)) is equivalent to (2.1). Applying the remaining triple integration $\int_0^1 \int_0^y \int_0^{y_3} \mathrm{d}y_2\,\mathrm{d}y_3\,\mathrm{d}y$ to (A3) is also equivalent to applying that to (2.1), which is the exact derivation of the FIK identity by Fukagata *et al.* (2002). Consequently, the fourfold integration of the mean vorticity equation reduces Yoon's identity to the FIK identity.

Appendix B. Reduce identity (2.4) to the FIK identity

To transform (2.4) to the FIK identity, we first rewrite (2.4) (by substituting (2.2)) as

$$C_f = 2\langle -u'v'\rangle + \frac{2}{Re_b}\frac{\mathrm{d}\langle u\rangle}{\mathrm{d}y} + yC_f. \tag{B1}$$

Multiplying (B1) by $(1-y)$ and integrating it in y over $[0, 1]$, we obtain

$$\int_0^1 (1-y)^2 C_f \mathrm{d}y = 2\int_0^1 (1-y)\langle -u'v'\rangle\,\mathrm{d}y + \frac{2}{Re_b}\int_0^1 (1-y)\frac{\mathrm{d}\langle u\rangle}{\mathrm{d}y}\,\mathrm{d}y. \tag{B2}$$

Note that the second term in right-hand side of (B2) can be computed by integration by parts:

$$\int_0^1 (1-y)\frac{\mathrm{d}\langle u\rangle}{\mathrm{d}y}\,\mathrm{d}y = (1-y)\langle u\rangle\Big|_{y=0}^{y=1} + \int_0^1 \langle u\rangle\,\mathrm{d}y = 1. \tag{B3}$$

Then (B2) is simplified to

$$\frac{1}{3}C_f = 2\int_0^1 (1-y)\langle -u'v'\rangle\,\mathrm{d}y + \frac{2}{Re_b}, \tag{B4}$$

which is identical to the FIK identity (1.1).

Appendix C. Form of (2.4) in the case of turbulent pipe flows

A similar identity can be derived also in the case of turbulent pipe flows. In this appendix, some notation and symbols are different from the main text. We use x, r and θ to represent the streamwise, radial and azimuthal directions, respectively. Velocities in these three directions are u_x, u_r and u_θ. Corresponding vorticities are ω_x, ω_r and ω_θ. The angle bracket $\langle\rangle$ represents averaging over homogeneous directions (streamwise and azimuthal directions) and time. Here, R^* is the radius of the pipe and $Re_b = u_b^* R^*/\nu^*$ is the bulk Reynolds number. Variables without the superscript * represent non-dimensional quantities normalized by u_b^* and R^*. Wall-shear stress is written as $\tau_w^* = -\mu^*(\partial u_x^*/\partial r^*)|_{r=1}$. Notation and symbols without mentions are consistent with those in the main text.

We start from the dimensional streamwise mean momentum balance for fully developed incompressible turbulent pipe flows:

$$\frac{\mathrm{d}\langle -u_x' u_r'\rangle^*}{\mathrm{d}r^*} + \frac{\langle -u_x' u_r'\rangle^*}{r^*} - \frac{1}{\rho^*}\left\langle\frac{\partial p^*}{\partial x^*}\right\rangle + \nu^*\frac{1}{r^*}\frac{\mathrm{d}}{\mathrm{d}r^*}\left(r^*\frac{\mathrm{d}\langle u_x^*\rangle}{\mathrm{d}r^*}\right) = 0, \tag{C1}$$

where p^* is pressure. By the force balance in the streamwise direction, we have $-\pi R^{*2}\langle\partial p^*/\partial x^*\rangle = 2\pi R^*\langle\tau_w^*\rangle$. Substituting this relation into (C1), we obtain the non-dimensional equation

$$\frac{\mathrm{d}\langle -u_x' u_r'\rangle}{\mathrm{d}r} + \frac{\langle -u_x' u_r'\rangle}{r} - \frac{2}{Re_b}\frac{\mathrm{d}\langle u_x\rangle}{\mathrm{d}r}\bigg|_{r=1} + \frac{1}{Re_b}\left(\frac{1}{r}\frac{\mathrm{d}\langle u_x\rangle}{\mathrm{d}r} + \frac{\mathrm{d}^2\langle u_x\rangle}{\mathrm{d}r^2}\right) = 0. \tag{C2}$$

Like (2.2) in turbulent channel flows, there is also a decomposition of the turbulent inertia in the pipe flows:

$$\frac{\mathrm{d}\langle -u_x' u_r'\rangle}{\mathrm{d}r} + \frac{\langle -u_x' u_r'\rangle}{r} = \langle u_r\omega_\theta\rangle + \langle -u_\theta\omega_r\rangle. \tag{C3}$$

Substituting (C3) into (C2) and integrating in the radial direction from an arbitrary radius $r \in (0, 1)$ to $r = 1$ (wall surface), we get

$$\begin{aligned}&\int_r^1 \langle u_r\omega_\theta\rangle\,\mathrm{d}r + \int_r^1 \langle -u_\theta\omega_r\rangle\,\mathrm{d}r - \frac{1}{Re_b}\frac{\mathrm{d}\langle u_x\rangle}{\mathrm{d}r} - \frac{2}{Re_b}(1-r)\frac{\mathrm{d}\langle u_x\rangle}{\mathrm{d}r}\bigg|_{r=1}\\ &\quad + \frac{1}{Re_b}\int_r^1 \frac{1}{r}\frac{\mathrm{d}\langle u_x\rangle}{\mathrm{d}r}\,\mathrm{d}r + \frac{1}{Re_b}\frac{\mathrm{d}\langle u_x\rangle}{\mathrm{d}r}\bigg|_{r=1} = 0.\end{aligned} \tag{C4}$$

The skin-friction coefficient can be calculated by $C_f = -2(\mathrm{d}\langle u_x\rangle/\mathrm{d}r)|_{r=1}/Re_b$. Substituting it into (C4), we have

$$\begin{aligned}C_f = &\underbrace{2\int_r^1 \langle u_r\omega_\theta\rangle\,\mathrm{d}r}_{C_{f1}} + \underbrace{2\int_r^1 \langle -u_\theta\omega_r\rangle\,\mathrm{d}r}_{C_{f2}}\\ &\underbrace{-\frac{2}{Re_b}\frac{\mathrm{d}\langle u_x\rangle}{\mathrm{d}r}}_{C_{f3}} \underbrace{-\frac{4}{Re_b}(1-r)\frac{\mathrm{d}\langle u_x\rangle}{\mathrm{d}r}\bigg|_{r=1}}_{C_{f4}} + \underbrace{\frac{2}{Re_b}\int_r^1 \frac{1}{r}\frac{\mathrm{d}\langle u_x\rangle}{\mathrm{d}r}\,\mathrm{d}r}_{C_{f5}}.\end{aligned} \tag{C5}$$

This equation is another form of (2.4) in the case of turbulent pipe flows. The first four terms in the right-hand side of (C5) are similar to those in (2.4) with respect to

forms and interpretations. There is an additional term C_{f5}, whose appearance is due to the Laplacian operator in the cylindrical coordinates, as stated by Yoon *et al.* (2016). By virtue of $\langle u_x \rangle$ decreasing along the radial direction, C_{f5} contributes negatively to the skin friction. Similar to (2.4), the applicable scope of (C5) should satisfy: (i) the homogeneity in the streamwise and azimuthal directions, and (ii) the zero mean of u_r and u_θ at each radius.

Appendix D. Form of (2.4) in the case of turbulent boundary layer flows

In this appendix, we consider the case of turbulent boundary layer flows. The non-dimensional streamwise mean momentum balance for turbulent boundary layer flows is written as

$$-\frac{\partial\langle u^2\rangle}{\partial x}+\frac{\partial\langle -uv\rangle}{\partial y}-\left\langle\frac{\partial p}{\partial x}\right\rangle+\frac{1}{Re_\delta}\left(\frac{\partial^2\langle u\rangle}{\partial x^2}+\frac{\partial^2\langle u\rangle}{\partial y^2}\right)=0. \tag{D1}$$

The angle bracket $\langle\,\rangle$ used here represents averaging over spanwise direction and time. Additionally, p is pressure; $Re_\delta = u_0^*\delta^*/\nu^*$ is the Reynolds number; δ^* is the boundary-layer thickness (rather than the displacement thickness, as the asterisk means dimensional here) and u_0^* is the free stream velocity. Variables without the superscript * represent non-dimensional quantities normalized by u_0^* and δ^*. Notation and symbols without mentions are consistent with those in the main text.

The second term in the left-hand side of (D1) is not strictly equal to the turbulent inertia, but the error is negligible. We decompose it like the turbulent inertia, while there is a difference from that in channel flows (2.2) on account of the existence of the streamwise gradient:

$$\frac{\partial\langle -uv\rangle}{\partial y}=\langle v\omega_z\rangle+\langle -w\omega_y\rangle+\frac{1}{2}\frac{\partial}{\partial x}\langle u^2-v^2-w^2\rangle. \tag{D2}$$

Substituting (D2) into (D1), we get

$$\langle v\omega_z\rangle+\langle -w\omega_y\rangle+\frac{1}{Re_\delta}\frac{\partial^2\langle u\rangle}{\partial y^2}+\left\langle-\frac{\partial p}{\partial x}\right\rangle+I_x=0, \tag{D3}$$

where

$$I_x=\frac{1}{Re_\delta}\frac{\partial^2\langle u\rangle}{\partial x^2}-\frac{\partial\langle E\rangle}{\partial x} \tag{D4}$$

is an extra term owing to inhomogeneity in the streamwise direction, and $E=\frac{1}{2}(u^2+v^2+w^2)$ is the kinetic energy. Integrating (D3) in the wall-normal direction from 0 to an arbitrary height $y\in(0,\,1]$ and substituting $C_f=2(\partial\langle u\rangle/\partial y)|_{y=0}/Re_\delta$, we can obtain

$$C_f=\underbrace{2\int_0^y\langle v\omega_z\rangle\,\mathrm{d}y}_{C_{f1}}+\underbrace{2\int_0^y\langle -w\omega_y\rangle\,\mathrm{d}y}_{C_{f2}}+\underbrace{\frac{2}{Re_\delta}\frac{\partial\langle u\rangle}{\partial y}}_{C_{f3}}+\underbrace{2\int_0^y\left\langle-\frac{\partial p}{\partial x}\right\rangle\mathrm{d}y}_{C_{f4}}+\underbrace{2\int_0^y I_x\,\mathrm{d}y}_{C_{f5}}. \tag{D5}$$

This equation is another form of (2.4) in the case of boundary layer flows. The first three terms in the right-hand side of (D5) are similar to those in (2.4) with respect to forms and interpretations. Here, C_{f4} in (D5) represents contributions of pressure gradient to the skin friction and C_{f5} measures contributions of the inhomogeneous effect in the

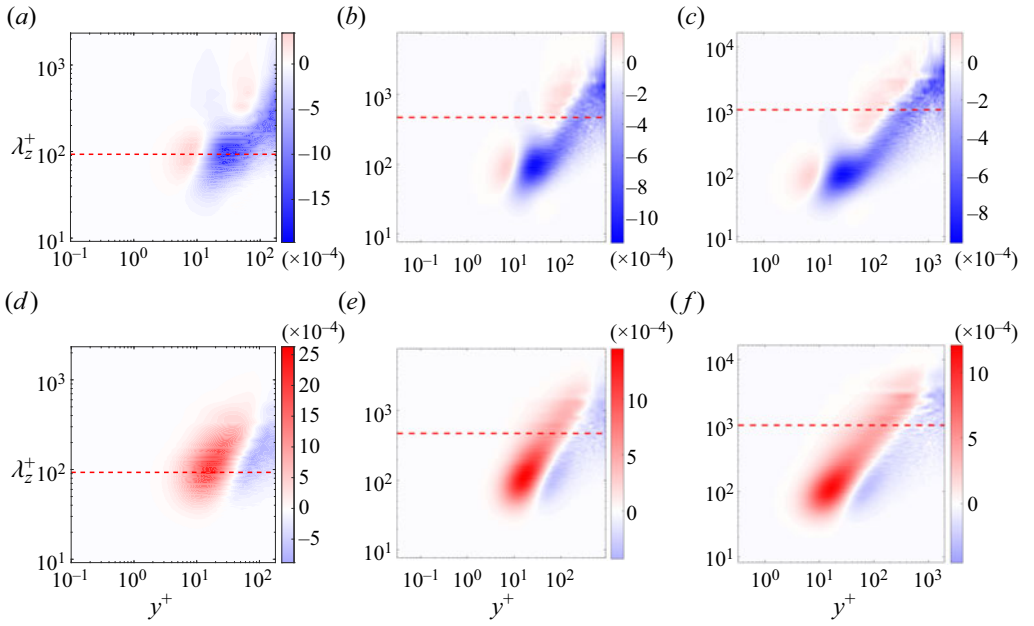

Figure 16. Pre-multiplied spanwise co-spectra (*a–c*) $yk_z\phi_{v\omega_z}$ and (*d–f*) $yk_z\phi_{-w\omega_y}$. (*a,d*) *Re*180; (*b,e*) *Re*950; (*c,f*) *Re*2000. The red dashed line indicates $\lambda_z^* = 0.5h^*$.

streamwise direction. Compared with (2.4), each decomposition term and C_f in (D5) are also functions of x, since we did not take the average over the streamwise direction. The applicable scope of (D5) should satisfy the homogeneity in the spanwise direction.

Appendix E. Filtering strategy using the constant cutoff wavelength

The cutoff wavelength $\alpha = 0.5$ is plotted as red dashed lines in pre-multiplied spanwise co-spectra of $v\omega_z$ and $-w\omega_y$, see figure 16. With respect to the co-spectra of velocity–vorticity correlations, coupling the dynamics of velocity and vorticity structures, the low-pass filter with this cutoff wavelength fails to properly extract the small- and large-scale motions, since the proportion of scales larger than $\lambda_z^* = \alpha h^*$ appears to merely change while part of the smaller scales keeps growing with the increase of Re_τ, regardless of different α.

Appendix F. Profiles of C_{fi}^{PS} and $C_{fi}^{NS}(i = 1, 2)$

Profiles of C_{f1} and C_{f2} in PSs and NSs are displayed in figure 17. Owing to the counteracting effect of positive and negative events in PSs, the range of C_{f1}^{PS} is smaller than C_{f1}^{NS}, indicating that C_{f1}^{NS} contributes to the majority of C_{f1}. In contrast, C_{f2}^{PS} contributes most to C_{f2}. By definition, NSs actually correspond to the local smaller-scale motions, which principally contribute negatively to C_f. However, it might not be a feasible approach to retard skin-friction drag by attempting to intensify motions in NSs (granted that this could be accomplished), since $C_{f1} + C_{f2}$ is essentially the Reynolds stress at height y (0 at $y = 1$) and when NSs are intensified, PSs will also come along to ensure the summation

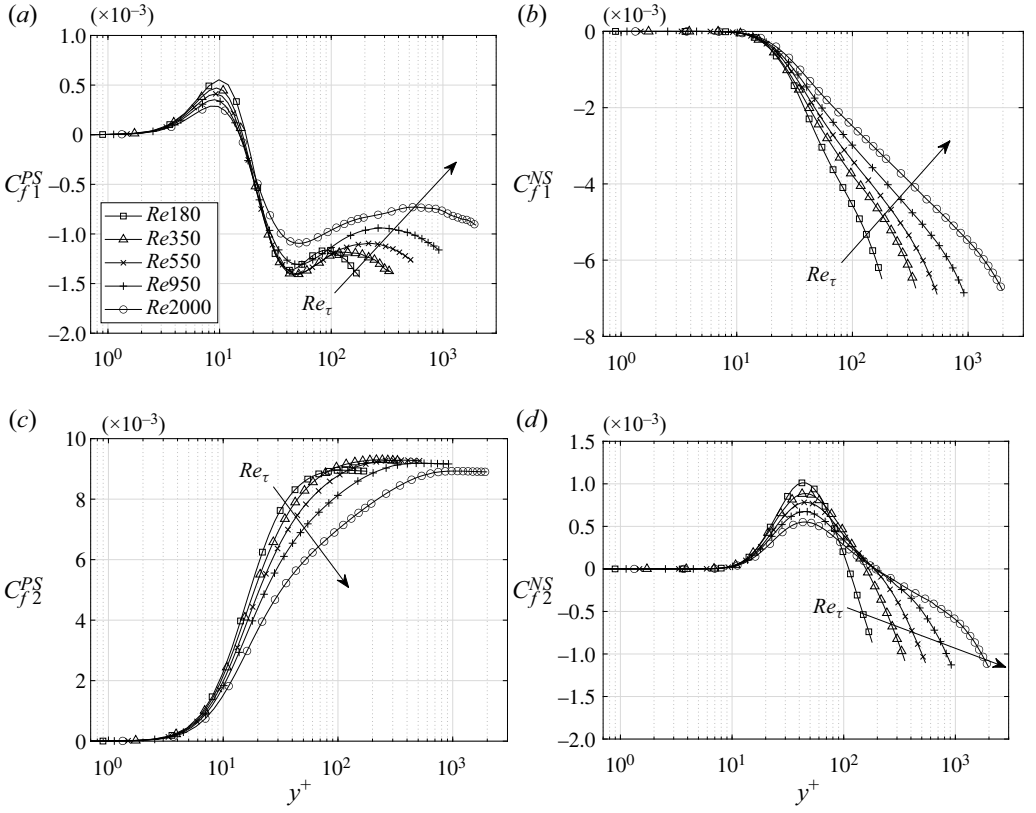

Figure 17. Profiles of (*a*) C_{f1}^{PS}, (*b*) C_{f1}^{NS}, (*c*) C_{f2}^{PS} and (*d*) C_{f2}^{NS} versus y^+.

is equal to the Reynolds stress. Now that the drag reduction strategy is not the issue of this work, we will not concentrate on this too much.

References

Bannier, A., Garnier, E. & Sagaut, P. 2015 Riblet flow model based on an extended FIK identity. *Flow Turbul. Combust.* **95**, 351–376.

Chan, C.I., Schlatter, P. & Chin, R.C. 2021 Interscale transport mechanisms in turbulent boundary layers. *J. Fluid Mech.* **921**, A13.

Cheng, C., Li, W., Lozano-Durán, A. & Liu, H. 2020 On the structure of streamwise wall-shear stress fluctuations in turbulent channel flows. *J. Fluid Mech.* **903**, A29.

Chin, C., Philip, J., Klewicki, J., Ooi, A. & Marusic, I. 2014 Reynolds-number-dependent turbulent inertia and onset of log region in pipe flows. *J. Fluid Mech.* **757**, 747–769.

Cho, M., Hwang, Y. & Choi, H. 2018 Scale interactions and spectral energy transfer in turbulent channel flow. *J. Fluid Mech.* **854**, 474–504.

De Giovanetti, M., Hwang, Y. & Choi, H. 2016 Skin-friction generation by attached eddies in turbulent channel flow. *J. Fluid Mech.* **808**, 511–538.

Dean, R.B. 1978 Reynolds number dependence of skin friction and other bulk flow variables in two-dimensional rectangular duct flow. *Trans. ASME J. Fluids Engng* **100** (2), 215–223.

Deck, S., Renard, N., Laraufie, R. & Weiss, P. 2014 Large-scale contribution to mean wall shear stress in high-Reynolds-number flat-plate boundary layers up to $\boldsymbol{Re_\theta} = 13\,650$. *J. Fluid Mech.* **743**, 202–248.

Del Álamo, J.C. & Jiménez, J. 2003 Spectra of the very large anisotropic scales in turbulent channels. *Phys. Fluids* **15** (6), L41–L44.

Del Álamo, J.C., Jiménez, J., Zandonade, P. & Moser, R.D. 2004 Scaling of the energy spectra of turbulent channels. *J. Fluid Mech.* **500**, 135–144.

DOOHAN, P., WILLIS, A.P. & HWANG, Y. 2021 Minimal multi-scale dynamics of near-wall turbulence. *J. Fluid Mech.* **913**, A8.

FAN, Y., ATZORI, M., VINUESA, R., GATTI, D., SCHLATTER, P. & LI, W. 2022 Decomposition of the mean friction drag on an NACA4412 airfoil under uniform blowing/suction. *J. Fluid Mech.* **932**, A31.

FAN, Y., CHENG, C. & LI, W. 2019*a* Effects of the Reynolds number on the mean skin friction decomposition in turbulent channel flows. *Z. Angew. Math. Mech.* **40** (3), 331–342.

FAN, Y. & LI, W. 2019 Review of far-field drag decomposition methods for aircraft design. *J. Aircraft* **56** (1), 11–21.

FAN, Y., LI, W., ATZORI, M., POZUELO, R., SCHLATTER, P. & VINUESA, R. 2020 Decomposition of the mean friction drag in adverse-pressure-gradient turbulent boundary layers. *Phys. Rev. Fluids* **5**, 114608.

FAN, Y., LI, W. & PIROZZOLI, S. 2019*b* Decomposition of the mean friction drag in zero-pressure-gradient turbulent boundary layers. *Phys. Fluids* **31** (8), 086105.

FUKAGATA, K., IWAMOTO, K. & KASAGI, N. 2002 Contribution of Reynolds stress distribution to the skin friction in wall-bounded flows. *Phys. Fluids* **14** (11), L73–L76.

GOMEZ, T., FLUTET, V. & SAGAUT, P. 2009 Contribution of Reynolds stress distribution to the skin friction in compressible turbulent channel flows. *Phys. Rev.* E **79**, 035301.

GUERRERO, B., LAMBERT, M.F. & CHIN, R.C. 2022 Precursors of backflow events and their relationship with the near-wall self-sustaining process. *J. Fluid Mech.* **933**, A33.

HOYAS, S. & JIMÉNEZ, J. 2006 Scaling of the velocity fluctuations in turbulent channels up to $\boldsymbol{Re_\tau} = 2003$. *Phys. Fluids* **18** (1), 011702.

HUTCHINS, N. & MARUSIC, I. 2007 Evidence of very long meandering features in the logarithmic region of turbulent boundary layers. *J. Fluid Mech.* **579**, 1–28.

HWANG, Y. 2013 Near-wall turbulent fluctuations in the absence of wide outer motions. *J. Fluid Mech.* **723**, 264–288.

HWANG, Y. 2015 Statistical structure of self-sustaining attached eddies in turbulent channel flow. *J. Fluid Mech.* **767**, 254–289.

JIMÉNEZ, J. 2018 Coherent structures in wall-bounded turbulence. *J. Fluid Mech.* **842**, P1.

KAMETANI, Y. & FUKAGATA, K. 2011 Direct numerical simulation of spatially developing turbulent boundary layers with uniform blowing or suction. *J. Fluid Mech.* **681**, 154–172.

KAMETANI, Y., FUKAGATA, K., ÖRLÜ, R. & SCHLATTER, P. 2015 Effect of uniform blowing/suction in a turbulent boundary layer at moderate Reynolds number. *Heat Fluid Flow* **55**, 132–142.

KLEWICKI, J.C. 1989 Velocity–vorticity correlations related to the gradients of the Reynolds stresses in parallel turbulent wall flows. *Phys. Fluids* A*: Fluid Dyn.* **1** (7), 1285–1288.

KLEWICKI, J.C. 2013 A description of turbulent wall-flow vorticity consistent with mean dynamics. *J. Fluid Mech.* **737**, 176–204.

LEE, M. & MOSER, R.D. 2019 Spectral analysis of the budget equation in turbulent channel flows at high Reynolds number. *J. Fluid Mech.* **860**, 886–938.

LI, W., FAN, Y., MODESTI, D. & CHENG, C. 2019 Decomposition of the mean skin-friction drag in compressible turbulent channel flows. *J. Fluid Mech.* **875**, 101–123.

LOZANO-DURÁN, A., BAE, H.J. & ENCINAR, M.P. 2020 Causality of energy-containing eddies in wall turbulence. *J. Fluid Mech.* **882**, A2.

LOZANO-DURÁN, A. & JIMÉNEZ, J. 2014 Effect of the computational domain on direct simulations of turbulent channels up to $\boldsymbol{Re_\tau} = 4200$. *Phys. Fluids* **26** (1), 011702.

MATHIS, R., MONTY, J.P., HUTCHINS, N. & MARUSIC, I. 2009 Comparison of large-scale amplitude modulation in turbulent boundary layers, pipes, and channel flows. *Phys. Fluids* **21** (11), 111703.

MEHDI, F., JOHANSSON, T.G., WHITE, C.M. & NAUGHTON, J.W. 2013 On determining wall shear stress in spatially developing two-dimensional wall-bounded flows. *Exp. Fluids* **55**, 1656.

MEHDI, F. & WHITE, C.M. 2011 Integral form of the skin friction coefficient suitable for experimental data. *Exp. Fluids* **50**, 43–51.

MEREDITH, P.T. 1993 Viscous phenomena affecting high-lift systems and suggestions for future CFD development. *High Lift Syst. Aerodyn. AGARD CP* **515**, 19.1–19.8.

MODESTI, D., PIROZZOLI, S., ORLANDI, P. & GRASSO, F. 2018 On the role of secondary motions in turbulent square duct flow. *J. Fluid Mech.* **847**, R1.

PEET, Y. & SAGAUT, P. 2009 Theoretical prediction of turbulent skin friction on geometrically complex surfaces. *Phys. Fluids* **21** (10), 105105.

PRIYADARSHANA, P.J.A., KLEWICKI, J.C., TREAT, S. & FOSS, J.F. 2007 Statistical structure of turbulent-boundary-layer velocity–vorticity products at high and low Reynolds numbers. *J. Fluid Mech.* **570**, 307–346.

RENARD, N. & DECK, S. 2016 A theoretical decomposition of mean skin friction generation into physical phenomena across the boundary layer. *J. Fluid Mech.* **790**, 339–367.

RICCO, P. & SKOTE, M. 2022 Integral relations for the skin-friction coefficient of canonical flows. *J. Fluid Mech.* **943**, A50.

SILLERO, J.A., JIMÉNEZ, J. & MOSER, R.D. 2013 One-point statistics for turbulent wall-bounded flows at Reynolds numbers up to $\delta^+ \approx 2000$. *Phys. Fluids* **25** (10), 105102.

TENNEKES, H. & LUMLEY, J.L. 1972 *A First Course in Turbulence*. MIT Press.

TOWNSEND, A.A. 1976 *The Structure of Turbulent Shear Flow*, 1st edn. Cambridge University Press.

WEI, T. 2018 Integral properties of turbulent-kinetic-energy production and dissipation in turbulent wall-bounded flows. *J. Fluid Mech.* **854**, 449–473.

WENZEL, C., GIBIS, T. & KLOKER, M. 2022 About the influences of compressibility, heat transfer and pressure gradients in compressible turbulent boundary layers. *J. Fluid Mech.* **930**, A1.

XIA, Z., ZHANG, P. & YANG, X.I.A. 2021 On skin friction in wall-bounded turbulence. *Acta Mechanica Sin.* **37**, 589–598.

XU, D., WANG, J. & CHEN, S. 2022 Skin-friction and heat-transfer decompositions in hypersonic transitional and turbulent boundary layers. *J. Fluid Mech.* **941**, A4.

YOON, M., AHN, J., HWANG, J. & SUNG, H.J. 2016 Contribution of velocity-vorticity correlations to the frictional drag in wall-bounded turbulent flows. *Phys. Fluids* **28** (8), 081702.

YOON, M., HWANG, J. & SUNG, H.J. 2018 Contribution of large-scale motions to the skin friction in a moderate adverse pressure gradient turbulent boundary layer. *J. Fluid Mech.* **848**, 288–311.

ZHANG, P. & XIA, Z. 2020 Contribution of viscous stress work to wall heat flux in compressible turbulent channel flows. *Phys. Rev.* E **102**, 043107.